How neuronal morphology impacts the synchronisation state of neuronal networks

Robert P Gowers[1,2,*], Susanne Schreiber[1,2,*]

[1] Institute for Theoretical Biology, Department of Biology, Humboldt-Universität zu Berlin, Philippstraße 13, Haus 4, 10115 Berlin, Germany

[2] Bernstein Center for Computational Neuroscience, 10115 Berlin, Germany

*** For correspondence:** robert.gowers@hu-berlin.de and s.schreiber@hu-berlin.de

Abstract

The biophysical properties of neurons not only affect how information is processed within cells, they can also impact the dynamical states of the network. Specifically, the cellular dynamics of action-potential generation have shown relevance for setting the (de)synchronisation state of the network. The dynamics of tonically spiking neurons typically fall into one of three qualitatively distinct types that arise from distinct mathematical bifurcations of voltage dynamics at the onset of spiking. Accordingly, changes in ion channel composition or even external factors, like temperature, have been demonstrated to switch network behaviour via changes in the spike onset bifurcation and hence its associated dynamical type. A thus far less addressed modulator of neuronal dynamics is cellular morphology. Based on simplified and anatomically realistic mathematical neuron models, we show here that the extent of dendritic arborisation has an influence on the neuronal dynamical spiking type and therefore on the (de)synchronisation state of the network. Specifically, larger dendritic trees prime neuronal dynamics for in-phase-synchronised or splayed-out activity in weakly coupled networks, in contrast to cells with otherwise identical properties yet smaller dendrites. Our biophysical insights hold for generic multicompartmental classes of spiking neuron models (from ball-and-stick-type to anatomically reconstructed models) and establish a direct mechanistic link between neuronal morphology and the susceptibility of neural tissue to synchronisation in health and disease.

Significance Statement

Cellular morphology varies widely across different cell types and brain areas. In this study, we provide a mechanistic link between neuronal morphology and the dynamics of electrical activity arising at the network level. Based on mathematical modelling, we demonstrate that modifications of the size of dendritic arbours alone suffice to switch the behaviour of otherwise identical networks from synchronised to asynchronous activity. Specifically, neurons with larger dendritic trees tend to produce more stable phase relations of spiking across neurons. Given the generality of the approach, we provide a novel, morphology-based hypothesis that explains the differential sensitivity of tissue to epilepsy in different brain areas and assigns relevance to cellular morphology in healthy network computation.

Introduction

Network states are instrumental for neural computation: they correlate with the behavioural state in healthy animals, such as in central pattern generator circuits for movement [1, 2], and are also often altered in neuropathologies [3, 4, 5]. Recent theoretical and experimental work highlights that it is not only the connectivity between neurons which plays a role in determining network behaviour, but that neuron-intrinsic properties also exert an influence [6, 7, 2]. Mechanistically, these influences arise not only from indirect effects on connectivity, such as plastic changes in synaptic transmission or modulation of plasticity rules, but also from direct effects on the very core of processing by a single neuron: the qualitative dynamics of action-potential generation that define a neuron's excitability class as described by Hodgkin [8]. Along these lines, weakly coupled inhibitory neurons with class 1 cell-intrinsic excitability do not foster synchronous network states [9], while neurons arranged in the same network topology with homoclinic-type action-potential generation favour in-phase synchronisation [10, 7]. Among the parameters that alter the cellular excitability class, we find those that directly affect ion channel dynamics, including channel composition, extracellular ion concentration, and modulators such as temperature [11, 12, 13, 10, 6, 14, 7]. However, these are not all.

Here, we explore the implications of a neuronal property that has received comparatively less attention in the context of network dynamics, presumably due to its more inflexible, less variable nature: neuronal morphology. Although previous work has shown that even passive dendritic

arbours can play an important role in processing inputs [15, 16, 17, 18], their effect on the network state has not yet been explored. We demonstrate that differences in the extent of dendritic arborisation alone are sufficient to induce network behaviour that is either synchronised, with stable phase relationships between neuronal firing, or asynchronous. Differences in neuronal morphology thus offer an interesting and previously underestimated explanation for the differential susceptibility of neuronal tissue to synchronisation and potentially pathological phenomena such as epileptiform activity or spreading depolarisation.

Our approach exploits the fact that the dynamics of regularly spiking neurons with all-or-none action potentials come in at least three qualitatively different flavours – hereafter referred to as dynamical spiking types – corresponding to the three different mathematical bifurcations that underlie the onset of spiking at threshold. Despite the large diversity of neuronal properties, including a zoo of ion channels that shape a cell's conductance portfolio as well as extrinsic modulators such as ionic concentrations and temperature, regular spiking in neurons is initiated by either a saddle-node on an invariant cycle (SNIC) bifurcation, a subcritical Hopf bifurcation (in conjunction with a fold of limit cycles bifurcation), or a saddle homoclinic orbit (HOM) bifurcation. The different spike onset dynamics of these dynamical spiking types have been shown to influence the temporal relationships of spikes across neurons in weakly connected networks [19, 20, 21]. Indeed, it is the combination of synaptic and cellular voltage dynamics that determines the state of the network, with the influence of cellular voltage dynamics being particularly pronounced in fast synaptic transmission. In this context, passive properties such as neuronal morphology also have an influence on the effective dynamics of spike generation. Larger dendritic branches induce a larger leak, which – as we demonstrate in this study – is sufficient to alter the dynamical spiking type, and consequently, the network synchronisation state.

Given the considerable heterogeneity between dendritic arbours — even in neurons of the same class and layer [22, 23, 24] — deciphering their influence on properties of neural computation and network states is a worthy endeavour. In this study, we methodically demonstrate that the morphology of dendritic arbours can, via their effect on a cell's input impedance, be tuned to promote (de)synchronisation of network activity. Using a neuron model of an active conductance-based soma attached to a passive dendrite, we first recapitulate how the input impedance differs between single-compartment and dendrite-and-soma models. We then show how to calculate the local bifurcation structure (and hence the dynamical spiking type) analytically when morphology is included. Of particular interest is the Bogdanov-Takens (BT) bifurcation, which acts

as an organising centre for different spiking onset bifurcations and hence dynamical types [25, 13]. In the next step, we show that the change in spike onset bifurcation from the dendritic load is reflected in the spiking timing response near the onset bifurcation. We further verify our results in detailed, anatomically reconstructed neuron models with varying degrees of dendritic arborisation, demonstrating that our results from the simplified dendrite-and-soma model are quantitatively precise, generalise and are widely applicable. Finally, we demonstrate the strong effect dendritic arborisation can have on network synchronisation via network simulations of multicompartment neurons of different dendritic extent, exemplifying the relevance of cellular morphology for the susceptibility of neuronal tissue to specific network states, including pathological dynamics.

Results

Passive Impedance Properties

Network behaviour is influenced by cellular properties of the constituent neurons via the dynamical spiking type they grant to each neuron. This is because distinct dynamical spiking types result in distinct timing sensitivities and consequently synchronisation properties of the network. Bringing neuronal morphology into play in a network environment therefore consists in first understanding how morphology impacts the dynamical spiking type.

Given that varying the speed at which the neuron's membrane potential changes has been shown to induce all known dynamical switches for regular spiking [13, 10], we start our investigation by analysing how dendrites affect temporal filtering of the neuron's membrane potential. To differentiate the voltage filtering effects caused by a dendritic arbour versus those captured by an isopotential point neuron, we first calculate the passive impedance properties of the single-compartment (S) and dendrite-and-soma models (DS). While the passive input impedance of an S model neuron is a first-order low-pass filter, spatial neuron models yield qualitatively different impedance profiles that depend on the dendritic properties [26, 27].

As we show in Figure 1, the DS model has an active soma attached to a passive dendrite which represents the equivalent cable of a branched dendritic arbour [28, 29]. If the active conductances in the soma have the same valued parameters and equations as the S model, then the two models differ only in their passive properties. The passive properties of the dendrite can be parametrised in terms of its length L, electrotonic length constant λ, passive time constant τ_δ, and dendritic dominance

factor ρ [29] (the ratio between the characteristic dendritic conductance and the somatic leak conductance).

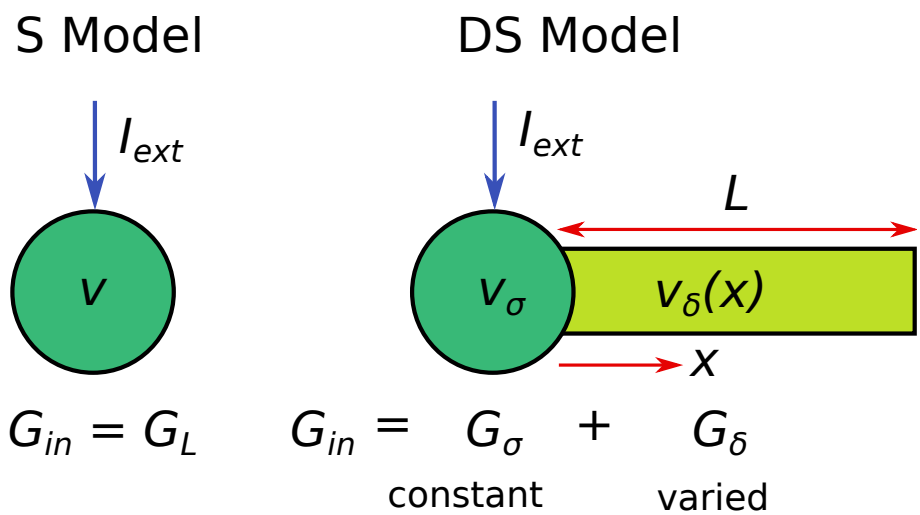

Figure 1. A comparison of the single-compartment (S) model with a dendrite-and-soma (DS) model with equivalent passive input conductance G_{in}. In the DS model, the constant input current I_{ext} is applied to the somatic compartment. In the S model, G_{in} is equivalent to the lumped leak conductance G_L, while for the DS model, G_{in} is the sum of the passive somatic (G_σ) and dendritic (G_δ) contributions. When we increase G_{in} in the DS model, G_σ is kept constant while G_δ is increased.

In this study, we vary the neuron's arborisation as captured by the dendritic contribution to the passive input conductance (G_δ). A neuron with more dendrites radiating from the soma will have a thicker equivalent cable and thus contribute more to the total passive input conductance G_{in}. The passive input conductance is given by the constant level of external input current I_{ext} required to change the voltage from its steady state value (when all active conductances are zero) by an amount Δv

$$I_{\text{ext}} = G_{\text{in}} \Delta v. \tag{1}$$

In the DS model, we apply I_{ext} to the soma and use the voltage change Δv at the soma for G_{in}. In each case G_{in} is the sum of its somatic (G_σ) and dendritic (G_δ) contributions. For a dendrite of effective length $\ell = L/\lambda$

$$G_{\text{in}} = G_\sigma + G_\delta = G_\sigma(1 + \rho \tanh \ell). \tag{2}$$

When $\ell \gg 1$, we can treat the dendrite as semi-infinite and the passive input conductance of the DS

model becomes

$$G_{\text{in}} = G_\sigma + G_\delta = G_\sigma(1+\rho). \tag{3}$$

For the S model $G_{\text{in}} = G_L$, the total leak conductance, allowing for a straightforward comparison between the two morphologies. While it is possible to adjust the dendritic parameters (ρ, λ, L) to match G_{in} for the S and DS models, this is not possible for the passive input admittance Y_{in} (the reciprocal of the input impedance, $Y_{\text{in}} \equiv Z_{\text{in}}^{-1}$). Denoting the angular frequency of the input signal as ω, for the S model Y_{in} is simply given as a first-order filter

$$Y_{\text{in}}^{\text{S}}(\omega) = G_L + i\omega C_{\text{m}}, \tag{4}$$

while for the semi-infinite and finite DS models we have

$$Y_{\text{in}}^{\text{F}}(\omega) = G_\sigma + i\omega C_\sigma + \rho G_\sigma \gamma(\omega)\tanh(\ell\gamma(\omega)), \tag{5}$$

$$Y_{\text{in}}^{\infty}(\omega) = G_\sigma + i\omega C_\sigma + \rho G_\sigma \gamma(\omega), \tag{6}$$

where $\gamma(\omega)$ is defined as

$$\gamma(\omega) = \sqrt{1 + i\omega\tau_\delta}. \tag{7}$$

This mismatch in the passive input admittance encapsulates the difference between the S and DS models, and we will explore the implications that it has on the neuronal dynamical spiking type. For the semi-infinite DS model, Y_{in} can be fully parametrised by G_{in} and τ_δ. From the form of Y_{in}, we see that τ_δ is a key parameter for comparing the DS and S models. When $\tau_\delta = 0$, $\gamma = 1$ at all frequencies and hence Y_{in}^F and Y_{in}^∞ become equal to Y_{in}^{S} in this limit for $G_{\text{in}} = G_L$. Thus the voltage dynamics of v_σ in the DS model become identical to the dynamics of v in the S model when $\tau_\delta = 0$.

We illustrate the differences between the passive input admittances of the S and DS models via its more commonly measured reciprocal, the input impedance Z_{in}. Figure 2A shows that for any given G_{in}, $|Z_{\text{in}}|$ is higher in the S model than the semi-infinite DS model at all non-zero frequencies. In Figure 2B, we see that $|Z_{\text{in}}|$ decreases at all non-zero frequencies when we increase τ_δ in the semi-infinite DS model. In the finite DS model, Figure 2C shows that if we hold G_{in} constant while decreasing ℓ, then $|Z_{\text{in}}|$ decreases at all non-zero frequencies.

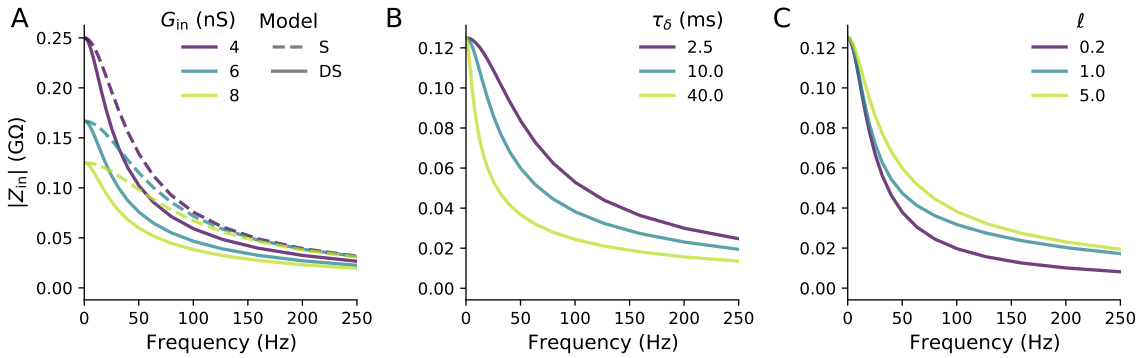

Figure 2. (**A**) When one fixes the input conductance G_{in} between the S model and a semi-infinite DS model, the magnitude of the input impedance Z_{in} will be higher for the S model for non-zero frequencies. $\tau_\delta = 10$ ms. (**B**) Increasing τ_δ of the DS model decreases $|Z_{\text{in}}|$ at all non-zero frequencies. $G_{\text{in}} = 8$ nS. (**C**) Decreasing the effective dendritic length ℓ while maintaining the same G_{in} also decreases $|Z_{\text{in}}|$ at all non-zero frequencies. $\tau_\delta = 10$ ms.

In our analyses of the DS model, we will vary directly G_{in} and τ_δ independently of each other rather than the underlying electrophysiological parameters they are defined in terms of (Equation 12). However, these parameter changes have various important biophysical interpretations. Firstly, increasing the dendritic diameter d increases G_{in} without affecting τ_δ. Additionally, τ_δ can be increased without altering G_{in} by increasing the dendritic membrane capacitance per unit area c_δ. Variations in the effective dendrite diameter between neurons can be significant and neuronal membrane capacitance per area may vary between mammalian species, though there are conflicting findings on this [30, 31].

While the two biophysical changes discussed so far are typically set once the neuron has developed and will not vary over short time scales, it is important to recognise that Y_{in} can be changed dynamically. One example of this is that increased synaptic bombardment distributed across the dendrite will increase the per-area leak conductance of the dendrite g_δ . This in turn will increase both G_{in} and decrease τ_δ [32, 33, 34]. Increasing d or decreasing g_δ also increases the length constant λ (Equation 12). For short dendrites, this is an important consideration, however for long dendrites with inputs applied to the soma, λ does not appear in Y_{in} or in any of the calculations of the local bifurcations as we show in the Methods section.

Bifurcation Structure

We now make the DS model active by giving the soma the dynamics of the Morris-Lecar model [35] while keeping the dendrite passive. The Morris-Lecar model was chosen because it has a single

time-dependent gating variable, making it one of the simpler conductance-based neuron models, and also because it has been extensively studied for its ability to change dynamical spiking type upon parameter variation [19, 36, 12, 37, 13]. We chose the default class I excitability parameter set of the Morris-Lecar model with $G_\sigma = 2$ nS, where details of the model's dynamics and parameters are given in the the Supporting Information.

Given that the DS model differs from the S model in terms of its passive input impedance, and that the input impedance can be fully described in terms of $(G_{\text{in}}, \tau_\delta)$ for the semi-infinite dendrite, it naturally follows that we should choose $(G_{\text{in}}, \tau_\delta)$ as bifurcation parameters along with I_{ext} in assessing the effect of morphology on the dynamical spiking type. Since the passive leak conductance in the soma $G_\sigma = 2$ nS, values of G_{in} above 2 nS denote the conductance load added to the neuron by the dendrite.

In Figure 3, we show several two-dimensional bifurcation diagrams in terms of $(I_{\text{ext}}, G_{\text{in}})$ plotted for various values of the third bifurcation parameter τ_δ. As discussed earlier in for the analysis of the input impedance, the case of $\tau_\delta = 0$ is equivalent to the S model where $G_{\text{in}} = G_L$. There are two saddle-node (SN) bifurcations at lower and higher I_{ext}, which we will hereafter refer to as "lower" and "higher" respectively. These two SN bifurcations converge at the cusp as G_{in} increases. Three fixed points exist for $I_{\text{ext}}^{\text{SN,low}} < I_{\text{ext}} < I_{\text{ext}}^{\text{SN,high}}$, one stable and two unstable. When spiking onset is caused by a SNIC bifurcation, this occurs on the higher SN bifurcation. These bifurcations are shown in black because they do not vary with τ_δ, and hence occur at exactly the same values of $(I_{\text{ext}}, G_{\text{in}})$ in the S and DS models.

For $\tau_\delta = 0$, the BT point is located on the higher SN bifurcation and has a subcritical Hopf bifurcation emerging from it. This Hopf bifurcation permits class II excitability. Thus the BT point has often been used heuristically as separating class I and class II excitability. Increasing τ_δ from zero initially shifts the BT bifurcation to higher G_{in} until it reaches the cusp at $\tau_\delta^{\text{BTC}} = 12.9$ ms (hereafter denoted as the BTC point). Increasing τ_δ beyond τ_δ^{BTC} moves the BT point onto the lower SN bifurcation curve and $G_{\text{in}}^{\text{BT}}$ now decreases as τ_δ increases. As the BT point passes the cusp as τ_δ increases, the criticality of the emerging Hopf bifurcation switches from subcritical to supercritical at the BTC point.

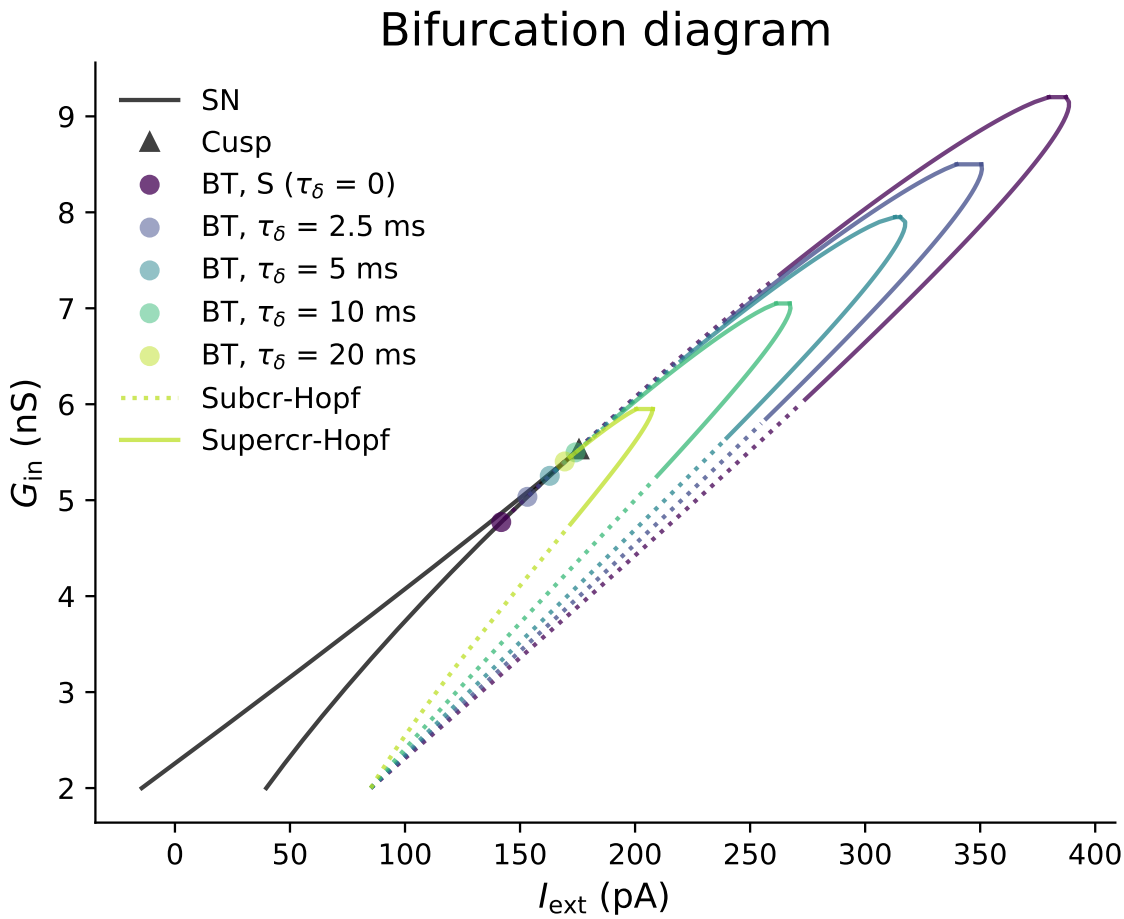

Figure 3. Two-parameter local bifurcation diagram in terms of $(I_{\text{ext}}, G_{\text{in}})$ of the Morris-Lecar DS model for various dendritic time constants τ_δ. At $\tau_\delta = 0$, the DS model is equivalent to an S model with a leak conductance of G_{in}. Increasing τ_δ shifts the BT bifurcation and shrinks the Hopf bifurcation curve. Initially increasing τ_δ moves the BT point to higher G_{in} until it reaches the cusp at the BTC point. Increasing τ_δ beyond τ_δ^{BTC} moves the BT point to the lower SN bifurcation curve and thus decreases $G_{\text{in}}^{\text{BT}}$. The Hopf bifurcation emerging from the BT point also switches from subcritical to supercritical when τ_δ passes the BTC point. The saddle-node and cusp bifurcations are shown in black because they are unaffected by changes to τ_δ.

When the Hopf bifurcation that emerges from the BT point is subcritical, it can be switched to supercritical by increasing G_{in}. This criticality switch moves to lower G_{in} as τ_δ increases towards τ_δ^{BTC}. At all τ_δ, there is a fold of Hopf bifurcations when G_{in} becomes sufficiently higher, and spiking is no longer possible at any applied current. The value of G_{in} for the fold of Hopf bifurcations decreases as τ_δ increases. The changes to the BT and Hopf bifurcations with τ_δ mean that we would expect the transition between class I and class II excitability to occur at higher G_{in} in the DS model for $\tau_\delta < \tau_\delta^{\text{BTC}}$.

To identify the input conductance for the SNIC to HOM switch, we must look at the saddle-node-loop (SNL) bifurcation [38, 39, 40, 10]. In Figure 4, we show the bifurcation types responsible for dynamical switching as a function $(\tau_\delta, G_{\text{in}})$. For all τ_δ, $G_{\text{in}}^{\text{SNL}} < G_{\text{in}}^{\text{BT}}$, with SNIC onset for $G_{\text{in}} < G_{\text{in}}^{\text{SNL}}$. The limit cycle formed by the HOM bifurcation in this case contains all three fixed points of the system (big-HOM). Since the SNL bifurcation converges to the BTC point, it therefore makes sense that $G_{\text{in}}^{\text{SNL}}$ also increases with τ_δ when $\tau_\delta < \tau_\delta^{\text{BTC}}$. Indeed, this is what we see in Figure 4, with not only $G_{\text{in}}^{\text{SNL}}$ increasing with τ_δ but also the conductance difference between the BT and SNL points decreasing before eventually converging at τ_δ^{BTC}. Thus both the SNIC $\rightarrow$ HOM switch and the G_{in} range for homoclinic onset are affected by the dendritic time constant. For $\tau_\delta > \tau_\delta^{\text{BTC}}$, we do not find an SNL bifurcation until τ_δ becomes large (not shown).

Strictly speaking there can exist another global bifurcation in the region $G_{\text{in}}^{\text{SNL}} < G_{\text{in}} < G_{\text{in}}^{\text{BT}}$ for which a fold of limit cycles (FLC) appears with a bifurcation current $I_{\text{ext}}^{\text{FLC}} < I_{\text{ext}}^{\text{HOM}}$, thus making the FLC the onset bifurcation [41, 13]. While this bifurcation can determine the switch between class I and class II excitability, we neglect to show it for the following reasons: (1) the spike timing perturbation response for FLC onset in this region is extremely similar to HOM onset; (2) though HOM onset in theory has class I excitability, its f–I curve is extremely steep at $I_{\text{ext}}^{\text{HOM}}$, making it hard to distinguish from class II excitability; and (3) the difference between $I_{\text{ext}}^{\text{FLC}}$ and $I_{\text{ext}}^{\text{HOM}}$ is typically extremely small [42] and thus $I_{\text{ext}}^{\text{HOM}}$ gives an accurate approximation of the onset current in this region. Thus due to simplicity and the high degree of functional similarity, we refer to the onset type for the whole of $G_{\text{in}}^{\text{SNL}} < G_{\text{in}} < G_{\text{in}}^{\text{BT}}$ as being HOM.

We see that some bifurcations are affected by τ_δ while others are not. Both the SN and cusp bifurcations are calculated from the existence of fixed points alone, and so the timescale of the dynamics (such as from τ_δ) will not affect them. On the other hand, the Hopf and BT bifurcations involve the stability switch of fixed points, for which knowledge of the timescale of the dynamics is necessary. For the SNL bifurcation, one can extend the reasoning in [10] to show that changing the timescale of the dynamics will break any existing homoclinic orbits at a given G_{in}. As a result, one would expect that changing τ_δ changes the value of $G_{\text{in}}^{\text{SNL}}$.

Our bifurcation analysis indicates that switching between dynamical spiking types can be induced by increasing the dendritic arborisation as parametrised by G_{in}. The switching between dynamical spiking types is qualitatively similar to increasing G_L in the single-compartment model, however the G_{in} values for the SNIC $\rightarrow$ HOM switch and subcritical Hopf onset increase with τ_δ, whilst the value of G_{in} for supercritical Hopf onset decreases with τ_δ.

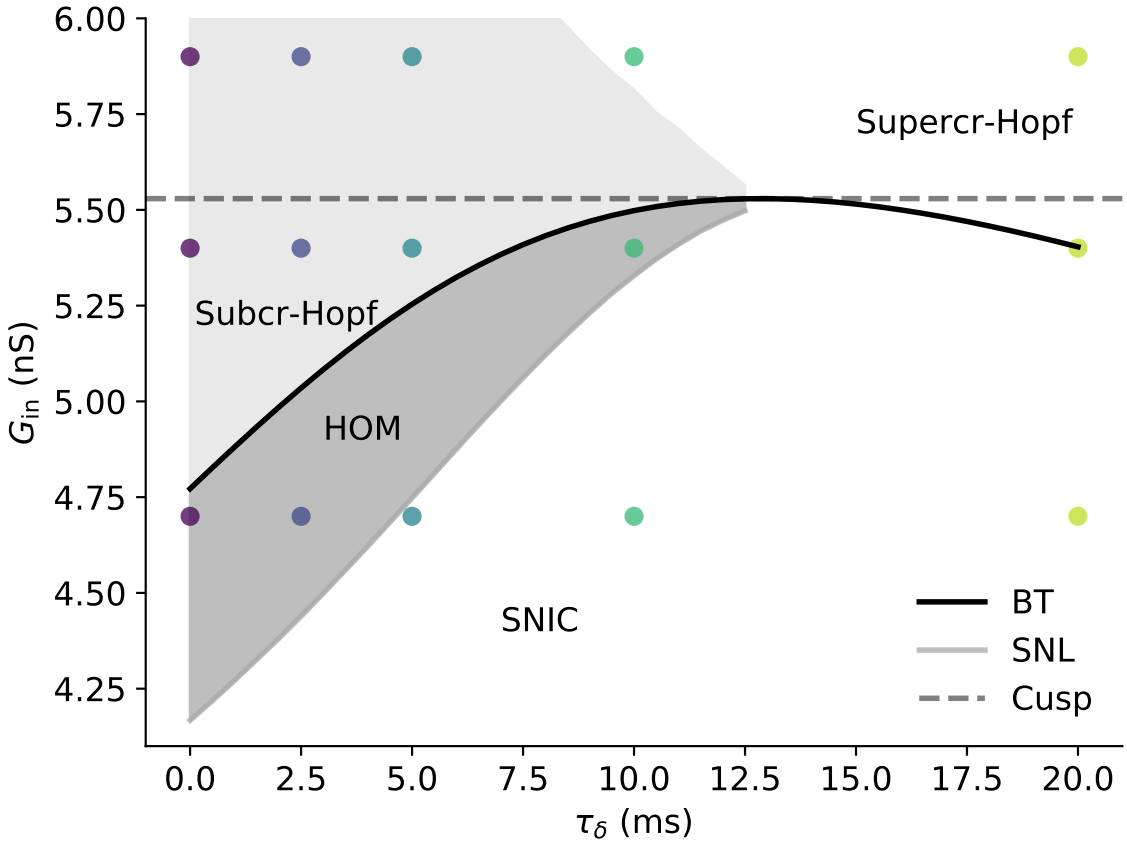

Figure 4. Bifurcation diagram of the Morris-Lecar DS model in terms of $(\tau_\delta, G_{\text{in}})$ focussing on dynamical switches. Here we have taken I_{ext} as the onset current for every value of $(\tau_\delta, G_{\text{in}})$. Points indicate values of $(\tau_\delta, G_{\text{in}})$ we later use for the spike timing response. At the saddle-node loop (SNL) bifurcation, the dynamical spiking type switches from SNIC to HOM, while Hopf onset becomes possible at the BT bifurcation. Increasing τ_δ above zero increases both $G_{\text{in}}^{\text{SNL}}$ and $G_{\text{in}}^{\text{BT}}$ until the BT and SNL bifurcations meet the cusp at the BTC point at τ_δ^{BTC}. The difference between $G_{\text{in}}^{\text{BT}}$ and $G_{\text{in}}^{\text{SNL}}$ decreases as τ_δ increases, meaning that the range of G_{in} for which HOM onset exists becomes smaller. For $\tau_\delta > \tau_\delta^{\text{BTC}}$, the SNL bifurcation no longer exists and $G_{\text{in}}^{\text{BT}}$ decreases. Furthermore, the Hopf onset for $G_{\text{in}} > G_{\text{in}}^{\text{BT}}$ switches from subcritical to supercritical. G_{in} for subcritical Hopf onset increases with τ_δ until τ_δ^{BTC}, while G_{in} for supercritical Hopf onset decreases with τ_δ throughout the whole range.

Phase-Response Curves

The dynamics of a neuronal spike affects how the neuron responds to external perturbations, which can come from chemical synapses, gap junction coupling, local field potentials, or externally applied currents. This has been found in both experimental [43, 44] and in modelling studies [45, 19]. The change in spike time caused by a perturbation to a tonically spiking neuron is described by the phase-response curve (PRC). In many cases, such as when neurons are weakly coupled or subject to

weakly correlated inputs, one can use an individual neuron's PRC to infer synchronisation conditions and the overall network state [19, 20, 21]. To see how the different dynamical spiking types affect the neuron's spiking response, we calculated the PRCs for the S and DS models for a range of (G_{in}, τ_δ). We chose the ($G_{\text{in}}, \tau_\delta$) values to be in the neighbourhood of the SNL, BT, and cusp bifurcations, as shown by the coloured points in Figure 4.

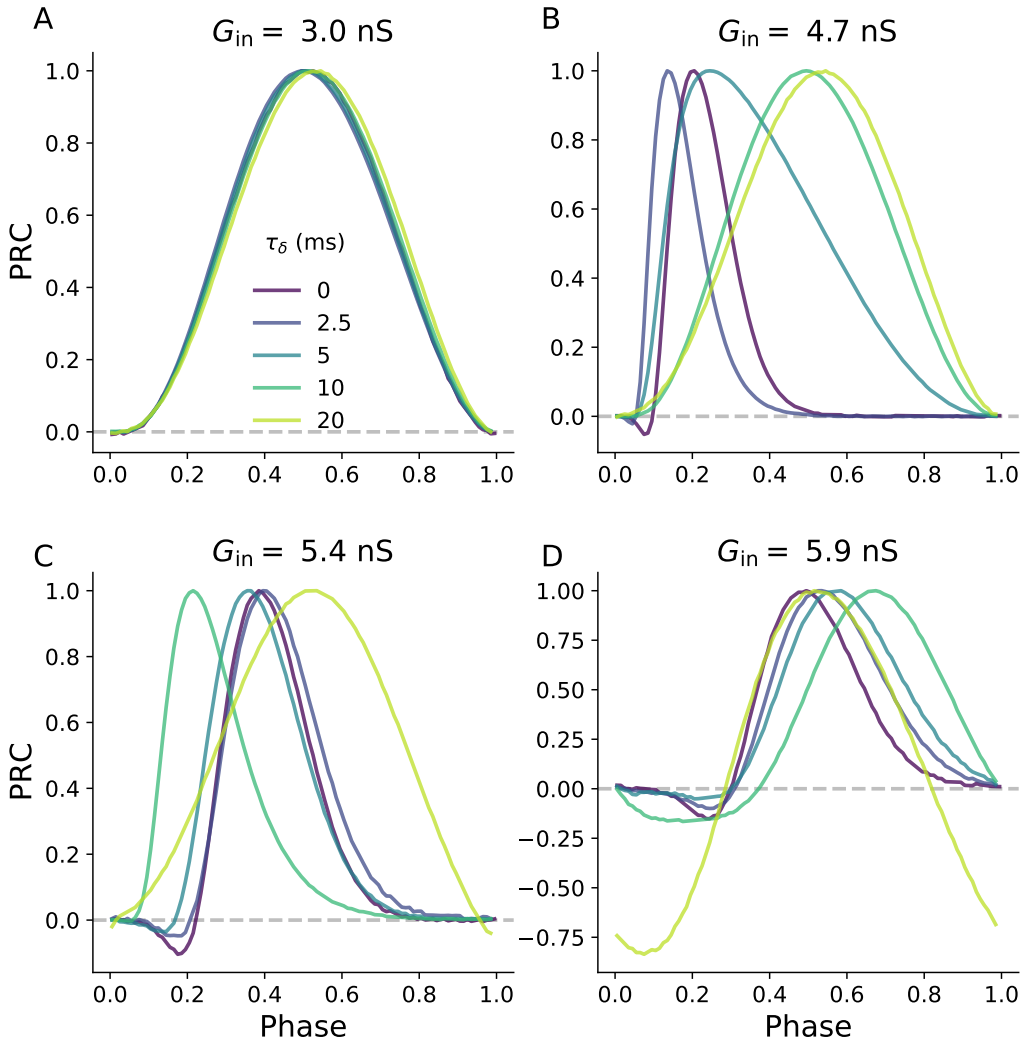

Figure 5. Phase-response curves (PRCs) of the Morris-Lecar DS model for various τ_δ and G_{in}. Values of G_{in} and τ_δ have been chosen to be around the dynamical switches in the Morris-Lecar DS model. For example at $\tau_\delta = 0$, $G_{\text{in}}^{\text{BT}} = 4.77$ nS and for all τ_δ the cusp bifurcation lies at $G_{\text{in}}^{\text{C}} = 5.53$ nS. When $\tau_\delta < \tau_\delta^{\text{BTC}}$ ($\tau_\delta^{\text{BTC}} = 12.9$ ms), increasing G_{in} switches the onset PRC shape first from a symmetric SNIC PRC (**A**) to an asymmetric HOM PRC (**B-C**), and later to a Hopf-like PRC (**D**). Increasing τ_δ increases the value of G_{in} at which the SNIC $\rightarrow$ HOM transition occurs and also decreases the G_{in} value of the HOM $\rightarrow$ Hopf transition. For $\tau_\delta > \tau_\delta^{\text{BTC}}$, the PRC transitions straight from SNIC to Hopf-like. DS parameters used $\ell = 5$.

At $G_{\text{in}} = 3$ nS, the Morris-Lecar neuron has SNIC spiking onset for all τ_δ. Hence Figure 5A shows symmetric positive-valued at this input conductance. At $G_{\text{in}} = 4.7$ nS (Figure 5B), the neuron is operating in the HOM regime for lower τ_δ and thus we see asymmetric positively-skewed PRCs associated with HOM onset [46, 10, 47], while for higher τ_δ the SNL bifurcation has not yet been reached and we still have symmetric SNIC PRCs. Further increasing G_{in} (Figure 5C) causes the neuron with $\tau_\delta = 10$ ms to pass its SNL point, inducing an asymmetric HOM PRC, while the PRC for $\tau_\delta = 20$ ms has negative regions after passing its BT bifurcation and adopting supercritical Hopf onset. Finally when G_{in} is above the cusp value (Figure 5D), all the neurons have Hopf onset with negative regions in their PRCs. However, the neuron with $\tau_\delta > 20$ ms has a far more sinusoidal PRC with a greater negative region due to its onset being via a supercritical rather than subcritical Hopf bifurcation.

Thus the procession of PRCs of the DS model as G_{in} is similar to the S model when $\tau_\delta < \tau_\delta^{\text{BTC}}$. For $\tau_\delta > \tau_\delta^{\text{BTC}}$, the asymmetric positive-valued PRC associated with HOM onset is not found, as predicted from the disappearance of the SNL bifurcation in the previous section. The G_{in} bifurcation values found earlier are thus useful predictors of the neuron's spiking response in the dendrite-and-soma model.

Full Morphology Test

To demonstrate that switches in the dynamical spiking type from increased input conductance are applicable to more complex and realistic neuronal morphologies, we calculated the PRCs from simulations of reconstructed dendritic arbours. In this case, we used the reconstructed dendritic arbour of a real Purkinje cell from NeuroMorpho.Org [48, 49]. We kept the somatic properties the same as the DS model investigated earlier and set all the dendritic compartments to have passive dynamics with $\tau_\delta = 2.5$ ms.

Starting with only the soma (representing the S model with default class I parameters), we increased G_{in} by adding dendritic compartments to reconstruct the full dendritic arbour in stages, as shown in the top row of Figure 6. At each stage of arborisation, we found the somatic onset current and measured the PRC. If we choose the G_{in} of the full dendritic arbour to be what would be in the subcritical Hopf regime of the DS model, then we can find different PRCs representing their respective dynamical spiking types by tuning the extent of dendritic arborisation. For instance, at the small arborisation in Figure 6A, G_{in} is low and we have a symmetric PRC indicative of SNIC

onset. Increasing G_{in} first gives rise to an asymmetric HOM-like PRC (Figure 6B-C) before eventually yielding a PRC with substantial negative regions representing Hopf onset (Figure 6D).

We then compared the detailed-morphology PRCs with PRCs obtained from an equivalent DS model. For this DS model, the dendritic length L and length constant λ were extracted for each stage of the Purkinje cell by reducing the arbour to an equivalent cable [28, 50]. Due to the different number of compartments between the detailed arbours and their DS equivalent models, we normalised the PRCs when comparing them by setting each PRC peak value to one. Figure 6 shows that the relative PRCs of the equivalent DS model in each stage agree very closely with the PRCs obtained from the full morphology, with small deviations of PRC peak location in the HOM region being the only noticeable difference.

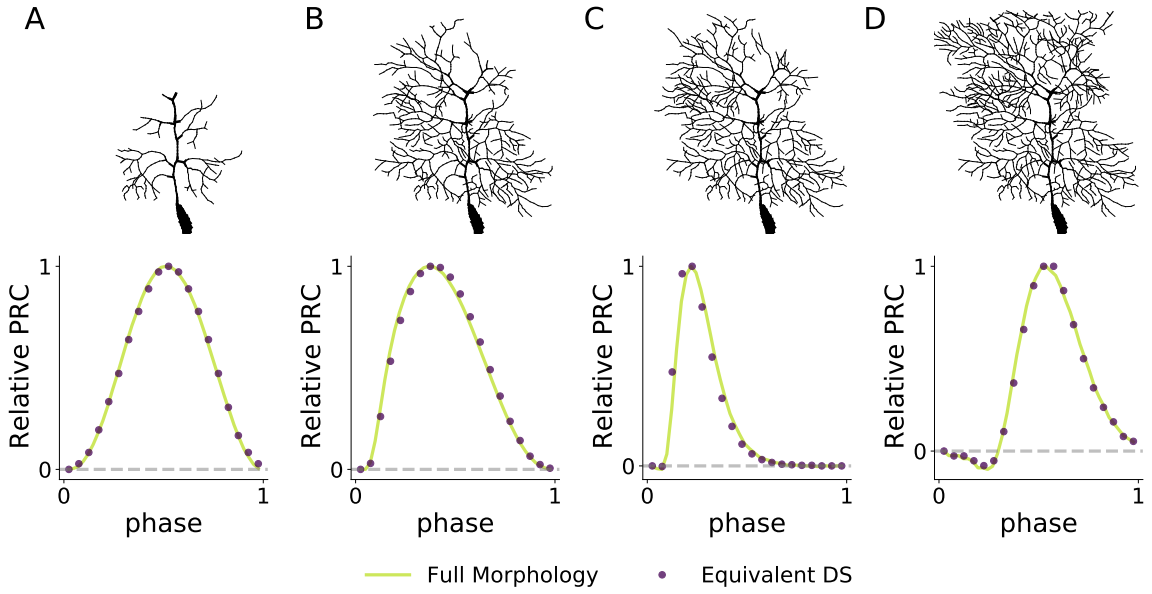

Figure 6. The PRCs obtained by simulating detailed multicompartment Purnkinje cell neuron show that the results of the simplified DS morphology are applicable to complicated and realistic dendritic arbours. Here we increase the input conductance of the multicompartment model by "growing" the dendritic arbour. We can see this switches the PRC shape from SNIC (**A**) to HOM (**B-C**) to Hopf (**D**) as in the DS model earlier. PRCs obtained from the equivalent DS model closely agree with the full morphology at each of the morphological stages.

While we have not attempted to accurately capture the complex active dynamics of Purkinje cells (whether in the soma or in the dendrites), we have used its highly branched and complex dendritic arbour to demonstrate that our modelling of a single equivalent dendrite and soma is adequate to approximately capture the affect on neuronal dynamical spiking type of realistic dendritic arbours. Our analysis is thus not limited to the equivalent dendrite morphology in the DS model, but is

applicable to realistic morphologies with highly bifurcated arbours with tapering dendrites.

Network Simulations

We now illustrate how the dendritic conductance load can affect the network synchronisation states of a small population of these neurons via a switch in dynamical spiking type. For a group of neurons where each member has a similar spiking frequency, we measure the synchronicity of the network by the scaled standard deviation of the phase differences ψ_i between the N neurons

$$R = \sqrt{\frac{N}{N-1}\left(\sum_{i=1}^{N} \psi_i^2 - \langle \psi \rangle\right)}. \tag{8}$$

For N neurons all synchronised in-phase, $R = 1$, while in the splayed-out state with $\psi_i = 1/N$ for all i, $R = 0$.

We simulated two separate networks each with 5 neurons with all-to-all connectivity of excitatory delta synapses. All synapses were connected to the soma of each neuron with zero transmission delay. In both networks the neurons had identical properties with a common dynamical spiking type: the first consisted of neurons with SNIC onset and the second of neurons with HOM onset. The synaptic strengths were chosen such that the maximum phase advance from a single synaptic input as predicted by the PRC is ~ 0.1, as shown in Figure 7D. The firing rate of each uncoupled neuron in both networks was set at 1 Hz. Thus the two networks differ in their dynamical spiking type and not the spiking frequency or the effective synaptic strength.

The first network consisted of neurons all with low dendritic load ($G_{\text{in}} = 3.45$ nS), placing them in the region of SNIC onset. We see in Figure 7A that the phase relations between neurons approaches a synchronous state but Figure 7C shows that this network does not settle to stable in-phase synchrony. The lack of a strongly attractive stable network spiking state for this network arises from the near-perfect symmetry of the SNIC PRC [9].

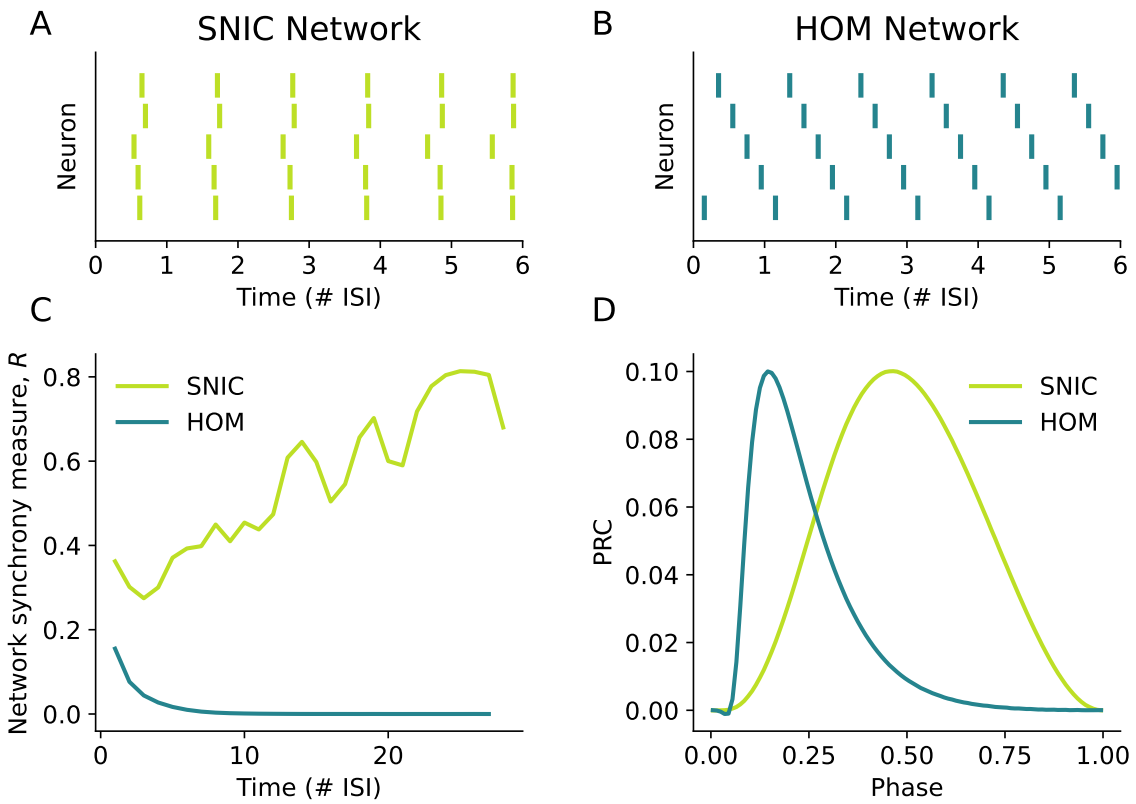

Figure 7. A comparison of two all-to-all networks with excitatory coupling between 5 neurons, one in which all the neurons have SNIC onset and the other in which all the neurons have HOM onset. Both networks had the same initial phase relations in the initial state with the final network states shown in (**A-B**). (**A**) The SNIC network almost achieves a synchronous network state, though this is weakly stable due to the near-symmetry of the PRC. (**B**) The HOM network achieves a splay state in which the neurons are phase-locked in which neuron i has a constant phase difference of $1/5$ with neuron $i+1$. (**C**) The synchrony measure over time shows that the SNIC network gradually and non-monotonically approaches the synchronous state while the HOM network converges to the splay state far more rapidly. In panels (**A-C**), time is measured in terms of the number of interspike-intervals (ISIs) of the network spiking rate. (**D**) The PRCs of each neuron in the SNIC and HOM networks.

By contrast, the second network consists of neurons all with higher dendritic load in the region of HOM onset ($G_{\text{in}} = 4.53$ nS). Figure 7B shows that this network converges to a splayed-out network spiking state which is approached rapidly as shown in Figure 7C. This splay state is made stable by the fact that the HOM PRC is asymmetric with a peak at a phase less than $1/N = 0.2$ [51].

Thus we have demonstrated how changes to the neuronal dynamics conferred by a more extensive neuronal morphology can affect the network behaviour. While these network states will be altered further by synaptic dynamics, transmission delays, and heterogeneities in neuronal properties, in the weak-coupling regime the neuron's PRC will remain an essential component in determining the

stable network states.

Discussion

In this article we have shown that not only can passive dendrites be included in the analysis of conductance-based neuron models, but also that the addition of a dendrite switches the dynamical spiking type of the neuron. In particular, we find that the reduction in input impedance caused by the dendrite can induce the SNIC $\rightarrow$ HOM dynamical switch, changing the onset PRC from symmetric to asymmetric. This dynamical spiking switch not only affects how information is processed within the individual neurons, it also implies that alterations in dendritic arborisation allow the network dynamics to achieve stable (de)synchronisation states. Specifically, our network simulations show that neurons with greater dendritic load (i.e. more extensive dendritic arbours) can achieve splay states for excitatory coupling due to their HOM onset. In contrast, these splay states could not be achieved by neurons with lower dendritic load (i.e. smaller dendritic arbours) which had SNIC onset. Different network (de)synchronisation states can thus be achieved by tuning the passive dendritic properties common to all neurons. Moreover, out findings establish a direct relationship between the susceptibility of neural tissue to synchronous network states and the morphology of the cells involved, helping us to better understand principles of neural design as well as the effect of deviations thereof in neuropathologies.

Dendritic modelling studies of conductance-based models have been performed previously. These include investigation of the effect of dendritic load on the firing frequency [52] and burst firing [15], the effect of dendritic perturbations on spike timing [53, 54], and the effect of dendritic coupling between spike-generating zones in the same neuron [55]. However, the work presented here is the first of its kind that shows via bifurcation analysis how morphology alters the dynamical spiking type and ultimately the (de)synchronisation state of the network.

The differential effect on the local bifurcations and PRCs when comparing the single-compartment and dendrite-and-soma models has utility for reducing the number of compartments in neuronal models for larger network simulations. If the input conductance is far from that of the BT point in the SNIC onset, then a single-compartment model with leak conductance equal to the input conductance of the morphology is appropriate. However, if G_{in} is close to $G_{\mathrm{in}}^{\mathrm{BT}}$, then one must use more sophisticated approximations of the input impedance (for example [56, 57, 58]). Our method showing how to calculate $G_{\mathrm{in}}^{\mathrm{BT}}$ in spatially extended models thus

informs one when these more sophisticated approximations are required.

Our results also prompt the hypothesis that neuronal morphology may be one crucial factor for the differential susceptibility of brain areas to pathological network states like epileptiform activity or spreading depolarisation [5, 59]. This could occur in two related ways. Firstly, pathological spiking patterns have been produced in modelling studies of single cells by changing the spiking dynamics [59, 60]. Because we have shown that the dendritic impedance alters spiking dynamics, changing the dendritic arborisation could therefore move the dynamical state of the neuron to a pathological region (via a switch in its neuronal dynamical spiking type) where network synchrony is changed. Second, pathological behaviour is often associated with either surplus or insufficient synchronous activity [3, 4, 5]. Since we have shown that the dynamical spiking switches resulting from added dendritic leak affect (de)synchronisation states, it follows that dendritic arborisation may move the degree of network synchrony to or from a pathological state.

Presently there is much research interest in how dendrites contribute to neuronal computation. This has largely focused on how either the nonlinear active dendritic channels [61, 62, 63] or nonlinear dendritic synapses in conjunction with passive dendritic compartments [64] affect the voltage or firing rate at the soma (i.e. voltage or rate coding). In demonstrating how the passive dendritic contribution changes the dynamical spiking type generated by the spiking compartment, we have added insights on one additional mechanism how dendrites can affect the temporal encoding of neuronal networks.

Methodologically, bifurcation analysis allowed us to calculate important local bifurcations of the system from a model consisting of an active soma attached to a spatially continuous passive dendrite. This approach is not restricted to the Morris-Lecar model examined in this article, but to any conductance-based neuron model with independent voltage-activated ion channels (e.g. the Wang-Buzsáki model [65]). The calculation of the BT and BTC bifurcations enabled us to predict how the dendrite affects the dynamical type, as these bifurcations act as organising centres for different dynamical types and different switches between dynamical types respectively.

Specifically, using the external input current, passive input conductance and dendritic time constant as bifurcation parameters, we found that the dendrite differentially affects the local bifurcations of the system. The saddle-node and cusp bifurcations are unaffected by the dendritic time constant of the system, meaning that all dendrite-and-soma models have the same saddle-node bifurcation locations as their corresponding single-compartment model with equivalent leak conductance. In contrast, the BT bifurcation moves in an “anticlockwise” direction about the cusp as

the dendritic time constant increases, with the emerging Hopf bifurcation switching from subcritical to supercritcal at the BTC bifurcation. This change in the BT bifurcation with the dendritic time constant demonstrated that the effect of passive dendritic load on the dynamical spiking type cannot be fully replicated with a single-compartment model with an increased leak conductance.

On a mathematical note, the "anticlockwise" shift in the BT bifurcation with increasing τ_δ meant that the switch between class I and class II excitability occurs at higher input conductances for $\tau_\delta < \tau_\delta^{\mathrm{BTC}}$. Furthermore, it means that the switch between SNIC and HOM onset at the SNL bifurcation occurs at higher input conductances, and that the input conductance region of HOM onset is smaller. Examining the PRCs confirmed the predicted spiking onset types from the bifurcation analysis: the SNIC $\rightarrow$ HOM switch is shifted to higher G_{in} when τ_δ is increased in the Morris-Lecar model. When τ_δ is above the BTC value, the HOM PRC region was eliminated.

Interestingly, the temporal sensitivity of neurons, as captured by the PRCs obtained from the morphologically detailed Purkinje cell reconstruction and its simplified DS model demonstrated the quantitative validity of our reduction approach in the earlier part of the analysis: PRCs of reconstructed neurons and those from the reduction of the dendritic arbour to a single equivalent cylinder were in excellent agreement. This demonstrates that the dynamical spiking type of a morphologically detailed neuron with passive dendrites can be predicted by knowing just its equivalent dendrite reduction and its active spike-generating currents. Furthermore, the equivalent dendrite reduction implies that an arbour that has more dendrites branching off the soma and thicker dendrites will have a greater impact on the neuron's dynamical spiking type.

We note that this work also establishes a framework from which other influences of the dendritic arbour on a neuron's spiking dynamics can be explored. As a first example, it allows us to analyse the effect of inputs applied to the dendrites. For a steady external current applied at an arbitrary location, our approach to calculating the local bifurcation structure can still be applied, as detailed in the Supporting Information. Meanwhile for transient dendritic perturbations, the PRCs from dendritic input have been simulated and observed experimentally in previous studies [17, 53, 54]. In these cases, it is found that the amplitude of the PRC decreases with the distance of the perturbation from the soma. On the other hand, the PRC shape is unchanged for positive-valued PRCs and is shifted for PRCs with negative-valued regions. Furthermore, background synaptic activity targeting the dendritic arbour also affects integrative properties of the neuron [32, 66, 67, 33, 34, 68]. This can be accommodated in our analysis via changes to the dendritic leak conductance and time constant.

The effect of some dendritic active currents can also, in principle, be included in our modelling

approach. If the currents are linearisable under the quasi-active approximation [69], then the effect of the active currents can included in the filtering properties of the dendrite [70, 55, 71, 72]. Weakly active dendritic currents, such as I_{h} and small-conductance Ca^{2+}-activated potassium current I_{SK}, have been found to change the PRCs from being positive-valued everywhere to having negative regions [54, 73], and thus may change the network synchronisation state. If the active currents are strong enough to elicit dendritic spikes [74], then this falls outside of the framework described in our work, firstly because there are now multiple spiking compartments, and second because the interaction between strong dendritic nonlinearities (e.g. spikes, plateau potentials) and axosomatic action potentials can induce bursting behaviour outside of the regular spiking regime [75, 76, 77]. However, some aspects of our work may still be used if one considers the strongly active dendritic region to be another oscillator coupled dendritically to the axosomatic compartment [55, 78].

Lastly, there has been much interest in how the geometry of the axonal initial segment (AIS) affects spike threshold and spike shape [79, 80, 81] and encoding of time-varying input [16, 82]. Extending our framework to include features of the axon, such as the spatial separation between the soma and the spike-initiation point on the AIS, would allow exploration of how the geometry of the system affects the dynamical spiking type. Changes in the dynamical type would in turn give further insight into how axonal geometry affects the neuron's temporal encoding of input.

In summary, we demonstrate that neuronal morphology can significantly influence the state of neuronal networks. Moreover, our results describe a method by which one can directly assess the impact of a dendritic arbour on neuronal excitability. Our approach is flexible in allowing for any conductance-based neuron model and external input currents applied to any location. Thus, the proposed approach enables further exploration of how dendritic arbour impacts the tuning of temporal encoding via changes to the network (de)synchronisation state. Our work highlights neuronal morphology as a contributor to neural function via changes to network synchrony, making it therefore likely that morphology is relevant for the differential sensitivity of neuronal tissue to synchronisation in health and disease.

Model and Methods

Active Soma and Passive Dendrite Model

A single-compartment (S) conductance-based neuron model consists of a leak current, B voltage-activated currents $I_{a,j}$ and an externally applied current I_{ext}

$$C_\sigma \frac{\mathrm{d}v}{\mathrm{d}t} = G_L(E_L - v) + \sum_{j=1}^{B} I_{\text{a},j}(\boldsymbol{a}_j, v) + I_{\text{ext}} = C_\sigma f_{\text{S}}(\boldsymbol{a}, v), \tag{9}$$

where each voltage-activated current depends on a set of activation/inactivation gating variables (hereafter termed "active variables"), $\boldsymbol{a}_j = (a_{j1}, ..., a_{jb_j})$. Altogether this gives K active variables indexed a_i from $i = 1, ..., K$. As in prior research regarding conductance-based models [13, 47, 6], we assume that the active variables are independent of each other and that their steady state distributions $a_{i,\infty}(v)$ saturate as $v \to \pm\infty$. Each active current has a reversal potential E_j, a maximal conductance G_j, and depends on the product of its active variables

$$I_{\text{a},j}(\boldsymbol{a}_j, v) = G_j(E_j - v) \prod_{i \in \boldsymbol{a_j}} a_i(v)^{p_i}, \tag{10}$$

where p_i is the gating exponent associated with active variable a_i. Finally, the each active variable evolves in time with a voltage-dependent time constant $\tau_i(v)$

$$\frac{\mathrm{d}a_i}{\mathrm{d}t} = \frac{a_{i,\infty}(v) - a_i}{\tau_i(v)} = f_{a,i}(a_i, v). \tag{11}$$

Using Rall's principle of an equivalent cylinder, a passive dendritic arbour emanating from the soma can be simplified to a single equivalent dendrite [28, 29]. We therefore modify the above model to include the dendritic morphology by attaching a passive equivalent dendrite to a conductance-based active soma. The dendrite is spatially continuous, with the coordinate x denoting the distance away from the soma and $v_\delta(x)$ denoting the dendritic potential at location x.

The dendrite is parametrised by its electrotonic length constant λ, its passive time constant τ_δ and the dendritic dominance factor ρ (the ratio between the characteristic dendritic conductance and the somatic leak conductance) [29]. These are each defined in terms of electrophysiological

parameters

$$\tau_\delta = \frac{c_\delta}{g_\delta}, \quad \lambda = \sqrt{\frac{d}{4r_a g_\delta}}, \quad \rho = \frac{\pi d g_\delta \lambda}{G_\sigma}, \tag{12}$$

where c_δ is the dendritic membrane capacitance per unit area, g_δ is the leak membrane conductance per unit area, r_a is the axial resistivity, d is the dendritic diameter and G_σ is the leak conductance of the soma.

Recalling that we denoted $\mathrm{d}v/\mathrm{d}t$ in (9) as f_S, this means that the somatic voltage v_σ evolves as

$$\frac{\mathrm{d}v_\sigma}{\mathrm{d}t} = f_\mathrm{S}(\boldsymbol{a}, v_\sigma) + \frac{\rho G_\sigma \lambda}{C_\sigma} \left.\frac{\partial v_\delta}{\partial x}\right|_{x=0}, \tag{13}$$

where the last term represents the axial current flowing from the dendrite to the soma.

The dendritic potential obeys the passive cable equation

$$\tau_\delta \frac{\partial v_\delta}{\partial t} = E_L - v_\sigma + \lambda^2 \frac{\partial^2 v_\delta}{\partial x^2}, \quad 0 < x < L, \tag{14}$$

where for simplicity we have assumed that the leak reversal potential is the same in the dendrite as the soma. The dendritic potential is subject to continuity of potential at $x = 0$ so $v_\delta(x = 0) = v_\sigma$, and a sealed-end boundary condition at $x = L$

$$\left.\frac{\partial v_\delta}{\partial x}\right|_{x=L} = 0. \tag{15}$$

Defining the electrotonically normalised length as $\ell = L/\lambda$, when $\ell \gg 1$, the distal dendritic end is too far away to be influenced by somatic activity, and we can simplify the model by making the dendrite semi-infinite in extent.

Calculation of Local Bifurcations

Here we will describe how the local bifurcations of the DS system can be calculated for any conductance-based soma model with $(I_\mathrm{ext}, G_\mathrm{in}, \tau_\delta)$ as the bifurcation parameters. Although we primarily focus on the semi-infinite dendrite in this article, the method we outline here can be adapted for the finite dendrite, as given in the Supporting Information. The equations we derive for each bifurcation are applicable to a spatially continuous dendrite rather than for a specific finite number of dendritic compartments.

Fixed Points

Since local bifurcations are defined by the properties of a fixed point, we first outline how to calculate fixed points of the DS system. The fixed points are defined as the values $(\boldsymbol{a}^*, \boldsymbol{v}^*)$ for which all time derivatives of the system (11, 13, 14) are equal to zero. From (11), each of the active variables satisfies $a_i^* = a_{i,\infty}(v_\sigma)$ at equilibrium. The cable equation of (14) at equilibrium becomes the second-order ODE

$$0 = E_L - v_\delta^* + \lambda^2 \frac{\mathrm{d}^2 v_\delta^*}{\mathrm{d}x^2}, \quad v_\delta^*(0) = v_\sigma^*, \quad \left.\frac{\mathrm{d}v_\delta^*}{\mathrm{d}x}\right|_{x=L} = 0. \tag{16}$$

This has the following solution in terms of v_σ

$$v_\delta^*(x) = E_L + (v_\sigma^* - E_L)\frac{\cosh[(L-x)/\lambda]}{\cosh(L/\lambda)}, \tag{17}$$

which in the semi-infinite limit reduces to

$$v_\delta^*(x) = E_L + (v_\sigma^* - E_L)e^{-x/\lambda}. \tag{18}$$

Thus all the active variables and the dendritic potential for all x at equilibrium are given in terms of the somatic resting potential v_σ^*. Defining the steady-state current as

$$I_\infty(v_\sigma^*) = C_\sigma f_{\mathrm{S}}(\boldsymbol{a}_\infty(v_\sigma^*), v_\sigma^*) + \rho g_\sigma \lambda \left.\frac{\mathrm{d}v_\delta^*}{\mathrm{d}x}\right|_{x=0}, \tag{19}$$

we can substitute in the dendritic voltage derivative at $x = 0$ to give in the semi-infinite case

$$I_\infty(v_\sigma^*) = C_\sigma f_{\mathrm{S}}(\boldsymbol{a}_\infty(v_\sigma^*), v_\sigma^*) + \rho G_\sigma (E_L - v_\sigma^*). \tag{20}$$

The somatic equilibrium potential v_σ^* is obtained by numerically solving $I_\infty = 0$. We note that the steady-state current equation (20) is the same as what we would find for the S model if $G_L = G_\sigma(1+\rho)$ as τ_δ is not present.

Saddle-Node (SN) Bifurcation

At a saddle-node bifurcation, a saddle and node fixed-point meet. Therefore we have a repeated root v_σ^{SN} of $I_\infty = 0$, which means at the saddle-node

$$\frac{\mathrm{d}I_\infty}{\mathrm{d}v_\sigma}(v_\sigma^{\mathrm{SN}}) = 0. \tag{21}$$

For codimension one bifurcations such as the saddle-node bifurcation, we choose I_{ext} as the bifurcation parameter as we are interested in the onset current for spiking. Hence we can numerically solve (21) to obtain v_σ^{SN} as it does not contain I_{ext}. $I_{\mathrm{ext}}^{\mathrm{SN}}$ is obtained by rearranging $I_\infty = 0$. Note that for the same G_{in}, (21) is also identical for both S and DS models.

Cusp Bifurcation

At the cusp, two saddle-node bifurcations meet. Thus, the cusp bifurcation satisfies the condition

$$\frac{\mathrm{d}^2 I_\infty}{\mathrm{d}v_\sigma^2}(v_\sigma^{\mathrm{C}}) = 0. \tag{22}$$

For codimension-two bifurcations such as the cusp, we will use $(I_{\mathrm{ext}}, G_{\mathrm{in}})$ as our bifurcation parameters. This is analogous to the prior use of (I_{ext}, g_L) in point-neuron models [13]. Since $I''_{\mathrm{ext}}(v_\sigma)$ does not depend on G_{in} or I_{ext}, we numerically solve (22) to obtain v_σ^{C}. $G_{\mathrm{in}}^{\mathrm{C}}$ and $I_{\mathrm{ext}}^{\mathrm{C}}$ are obtained from rearranging (21) and (20) respectively. As with the saddle-node bifurcation, the cusp bifurcation condition does not depend on τ_δ, thus for the same G_{in} the cusp bifurcation values will be the same for the S and DS models.

Hopf Bifurcation

At a Hopf bifurcation, a fixed-point changes stability and a limit cycle appears. The criticality of the Hopf bifurcation determines the stability of the limit cycle involved; at a subcritical Hopf bifurcation we have the transition: stable FP + unstable LC $\rightarrow$ unstable FP, whilst at a supercritical Hopf bifurcation we have: stable FP $\rightarrow$ unstable FP + stable LC.

The Jacobian evaluated at a Hopf bifurcation has two purely imaginary conjugate eigenvalues $\pm i\omega_{\mathrm{H}}$. Denoting the corresponding right-eigenvector as $\boldsymbol{q}$ and its complex conjugate as $\overline{\boldsymbol{q}}$, this means

that we have

$$\boldsymbol{J}\boldsymbol{q} = i\omega_{\mathrm{H}}\boldsymbol{q}, \quad \boldsymbol{J}\overline{\boldsymbol{q}} = -i\omega_{\mathrm{H}}\overline{\boldsymbol{q}}. \tag{23}$$

From this pair of equations, we can derive two simultaneous nonlinear equations in terms of $(v_\sigma^{\mathrm{H}}, \omega_{\mathrm{H}})$ for the discretised system. Then we take the continuum limit to obtain two nonlinear equations for the continuous dendrite for which further details are found in the Supporting Information. These equations can be obtained to find v_σ^{H} and then $I_{\mathrm{ext}}^{\mathrm{H}}$ is obtained from from $I_\infty = 0$.

Unlike all the previous bifurcations listed, the Hopf bifurcation depends on τ_δ. Therefore, we should expect the bifurcation values of the Hopf bifurcation to differ between the S and DS models. The criticality of the Hopf bifurcation can be calculated using the approach outlined in [83], as detailed in the Supporting Information.

Bogdanov-Takens (BT) Bifurcation

At the BT point, a saddle-node, Hopf and saddle-node homoclinic orbit (HOM) bifurcations meet. Since the global HOM bifurcation can also determine the spiking onset type of the neuron [40, 25, 10, 13], the BT point acts as an organising centre in two parameter dimensions for different spiking onset types. Varying the bifurcation parameters $(I_{\mathrm{ext}}, G_{\mathrm{in}})$ in the vicinity of the BT point can therefore induce spiking onsets associated with the three codimension one bifurcations that meet here.

The Jacobian of the system has two zero eigenvalues at the BT point. This means that $\boldsymbol{J}$ will have orthogonal left, $\boldsymbol{l}$, and right, $\boldsymbol{r}$, eigenvectors satisfying

$$\boldsymbol{l}\boldsymbol{J} = \boldsymbol{0}, \quad \boldsymbol{J}\boldsymbol{r} = \boldsymbol{0}, \quad \boldsymbol{l}\boldsymbol{r} = \boldsymbol{0}. \tag{24}$$

These equations can be reduced to a single equation

$$\sum_{i=1}^{K} (\alpha_0\tau_\delta + \tau_i)\,\frac{\partial f_{\mathrm{S}}}{\partial a_i}\frac{\mathrm{d}a_{i,\infty}}{\mathrm{d}v_\sigma} + 1 + \alpha_0\tau_\delta\frac{\partial f_{\mathrm{S}}}{\partial v_\sigma} = 0, \tag{25}$$

where for the semi-infinite dendrite $\alpha_0 = 1/2$. Since (25) has no dependence on our bifurcation parameters $(I_{\mathrm{ext}}, G_{\mathrm{in}})$, we can numerically solve it to find the equilibrium potential v_σ^{BT}. $G_{\mathrm{in}}^{\mathrm{BT}}$ can then be obtained by rearranging the saddle-node condition (21) and $I_{\mathrm{ext}}^{\mathrm{BT}}$ from the equilibrium condition $I_\infty = 0$. We again see that the BT bifurcation depends on τ_δ and thus we should expect

the location of the BT bifurcation to change with τ_δ.

Bogdanov-Takens-Cusp (BTC) Bifurcation

Finally, we outline how to find the BTC point. The BTC point is of particular interest because bifurcations associated with spike onset transitions coincide at this point. At a spiking onset transition, the spiking changes from one type to another. We should distinguish this from the lower codimension BT point by stating that the BT point organises bifurcations responsible for spiking onsets, while the BTC point organises bifurcations responsible for *transitions* of spiking onsets. The bifurcations that meet at the BTC point include the Bautin (where a Hopf bifurcation changes stability), neutral saddle-node (where a homoclinic bifurcation and a fold of limit cycles meet), saddle-node loop (where saddle-node and homoclinic bifurcations meet), and BT bifurcations [83, 25, 13].

Since the BTC point acts as an organising centre for spiking onset transitions, deviations in the bifurcation parameters around it will lead to variations in the spiking onset structure in two parameter dimensions. The BTC point also has the advantage of being easier to calculate than the global bifurcations which coalesce at it, as it is calculable from the properties of fixed-points.

The BTC point has codimension 3, meaning that its location must be expressed in terms of three bifurcation parameters. In the work of Kirst et al [13], an equation for the BTC point for point-neuron conductance-based models is given with $(I_{\text{ext}}, g_L, C_{\text{m}})$ as the bifurcation parameters, while in [6], Al-Darabsah and Campbell use the M-current conductance instead of C_{m}. Here we use the bifurcation parameters $(I_{\text{ext}}, \rho, \tau_\delta)$ as they are common to all conductance-based neuron models and it includes two dendritic parameters. Furthermore, τ_δ behaves similarly to C_{m}, in that increasing it slows the response of the dendrite to somatic activity.

As the BTC point is where a cusp and BT bifurcation coincide, one can use the cusp condition (22) to obtain the equilibrium voltage v_σ^{BTC}, the saddle-node condition (21) to give $G_{\text{in}}^{\text{BTC}}$, and the BT condition (25) to yield τ_δ^{BTC}.

Simulation Details

To simulate the DS models, a cable of length $L = 1000$ µm was discretised into $M = 50$ evenly spaced spatial compartments with step size $\Delta x = 20$ µm. The soma occupied a separate compartment at $x = 0$. All simulations utilised the DifferentialEquations.jl package [84] in the Julia

programming language [85], from which the Tsitouras 5/4 Runge-Kutta method was used.

For the SNL bifurcation and PRCs, we required an estimate of the onset current at which stable spiking begins. Here we used the value of I_{ext} which produced regular spiking at the lowest possible frequency above 1 Hz. This means that for class I onset the spiking frequency was approximately 1 Hz, while for class II onset this was typically greater.

At this onset current, PRCs were obtained by increasing the somatic potential by an amount Δv at a single time t_k corresponding to a phase θ_k. To ensure that the phase shift is approximately in the linear regime, Δv was chosen for each neuron such that the PRC maximum was never greater than 0.1. This procedure was repeated for input phases corresponding to $\theta_k = 0.01k - 0.005$, $k = 1, ..., 100$.

Code used to run all simulations, along with that used to calculate the local and global bifurcations, will be made available in the Supporting Information.

Acknowledgments

This project has received funding from the European Research Council (ERC) under the European Union's Horizon 2020 research and innovation program (grant agreement no 864243) and from the Einstein Foundation Berlin (EP-2021-621).

We would like to thank Jan-Hendrik Schleimer and Paul Pfeiffer for insightful discussions about excitability switching.

Supporting Information

Equations and Parameters of the Morris-Lecar Model

The single-compartment Morris-Lecar voltage equation is

$$f_{\text{S}}(n, v_\sigma) = \frac{1}{C_\sigma}\left[G_\sigma(E_L - v_\sigma) + m_\infty(v_\sigma)G_{\text{Ca}}(E_{\text{Ca}} - v_\sigma) + nG_{\text{K}}(E_K - v_\sigma) + I_{\text{ext}}\right], \tag{26}$$

while the dynamics of the recovery variable n are given by

$$\frac{\mathrm{d}n}{\mathrm{d}t} = \frac{n_\infty(v_\sigma) - n}{\tau_n(v_\sigma)}, \quad \tau_n(v_\sigma) = \left[\phi \cosh\left(\frac{v_\sigma - A_{\text{K}}}{4\Delta_{\text{K}}}\right)\right]^{-1}. \tag{27}$$

Steady-state values of the activation variables are given in terms of sigmoidal functions of v_σ

$$m_\infty(v_\sigma) = \left[1 + \exp\left(-\frac{v_\sigma - A_{\mathrm{Ca}}}{\Delta_{\mathrm{Ca}}}\right)\right]^{-1}, \quad n_\infty(v_\sigma) = \left[1 + \exp\left(-\frac{v_\sigma - A_{\mathrm{K}}}{\Delta_{\mathrm{K}}}\right)\right]^{-1} \tag{28}$$

Parameter	Value	Units
G_σ	2	nS
C_σ	20	pF
E_L	-60	mV
G_{Ca}	4	nS
E_{Ca}	120	mV
A_{Ca}	-1.2	mV
Δ_{Ca}	9	mV
G_{K}	8	nS
E_{K}	-80	mV
A_{K}	12	mV
Δ_{K}	8.7	mV
ϕ	1/15	ms^{-1}

Table 1. Default parameters used in this paper for the Morris-Lecar model, taken from [35] and scaled by a somatic area of 100 $\mu\mathrm{m}^2$.

Derivation of the Local Bifurcation Equations

The Method of Lines

For finite-dimensional dynamical systems, such as conductance-based point-neuron models, the Jacobian of the system has a finite number of eigenvalues. This gives a clear, but by no means trivial, approach to calculating the Hopf, BT and BTC bifurcations [10, 13, 6]. However, for a spatially continuous system, the number of dimensions is not finite. Fortunately, by using the method lines, we can derive equations for the bifurcations in an analogous fashion.

The method of lines discretises a spatially continuous system by dividing the cable into M compartments with index $k = 1, .., M$ [86]. In this case, we will use a constant spatial step size Δx such that $v_\delta(k\Delta x, t) = v_k(t)$ and use the following discretised approximations of the first and second-order spatial derivatives

$$\frac{\partial^2 v_k}{\partial x^2} \approx \frac{v_{k+1} - 2v_k + v_{k-1}}{\Delta x^2}, \quad \frac{\partial v_k}{\partial x} \approx \frac{v_{k+1} - v_k}{\Delta x}. \tag{29}$$

Note that $v_{k=0} = v_\sigma$ and that we must incorporate the sealed-end boundary condition, which

changes the second derivative approximation at the distal dendritic end to

$$\frac{\partial^2 v_M}{\partial x^2} \approx \frac{2v_{M-1} - 2v_M}{\Delta x^2}. \tag{30}$$

This discretisation means that we now have a $M + K + 1$ dimensional dynamical system, where we recall that K is the number of active variables. The active variable equations remain unchanged from (11), while the voltage equations in the discretised system are

$$\begin{aligned} \frac{\mathrm{d}v_\sigma}{\mathrm{d}t} &= f_{\mathrm{S}}(\boldsymbol{a}, v_\sigma) + \frac{\rho G_\sigma \lambda}{C_\sigma \Delta x}(v_1 - v_\sigma), \\ \frac{\mathrm{d}v_k}{\mathrm{d}t} &= \frac{E_L - v_k}{\tau_\delta} + \lambda^2 \frac{v_{k+1} - 2v_k + v_{k-1}}{\Delta x^2 \tau_\delta}, \quad k = 1, ..., M-1 \\ \frac{\mathrm{d}v_M}{\mathrm{d}t} &= \frac{E_L - v_M}{\tau_\delta} + \lambda^2 \frac{2v_{M-1} - 2v_M}{\Delta x^2 \tau_\delta}. \end{aligned} \tag{31}$$

From (11) and (31) we can obtain the Jacobian $\boldsymbol{J}$ for the discretised system, allowing us to approach the problem of calculating the local bifurcations in a similar manner to the point-neuron model. Although the Jacobian now has $(M + K + 1) \times (M + K + 1)$ elements, most of these are zero, and those associated with the dendritic equations do not depend on the state variables. Further details of this approach are given in the Appendix, but it is sufficient here to say that the method of lines allows local bifurcations to be calculated for the *discretised* dendrite-and-soma model. With the equations from the discretised dendrite, we can go further and take the continuum limit ($\Delta x \to 0$) to yield equations for the spatially *continuous* DS model. It is these spatially continuous bifurcation values which we show in the bifurcation diagrams.

With the method of lines established, we can now describe how to calculate the Hopf, BT and BTC bifurcations in a spatially continuous DS model.

Discretised Jacobian Matrix

Upon discretising the dendrite into M compartments each of width Δx, we have the following $M+K+1$ differential equations for the system

$$\frac{\mathrm{d}a_i}{\mathrm{d}t} = f_{ai}(a_i, v_\sigma) = \frac{a_{i,\infty}(v_\sigma) - a_i}{\tau_i(v_\sigma)}, \quad i = 1, ..., K, \tag{32}$$

$$\frac{\mathrm{d}v_\sigma}{\mathrm{d}t} = f_\sigma(\boldsymbol{a}, \boldsymbol{v}) = f_{\mathrm{S}}(\boldsymbol{a}, v_\sigma) + \frac{\lambda \rho G_\sigma}{\Delta x C_\sigma}(v_1 - v_\sigma), \tag{33}$$

$$\frac{\mathrm{d}v_k}{\mathrm{d}t} = f_k(\boldsymbol{v}) = \frac{E_L - v_k}{\tau_\delta} + \frac{\lambda^2}{\Delta x^2 \tau_\delta}(v_{k-1} - 2v_k + v_{k+1}), \quad k = 1, ..., M-1 \tag{34}$$

$$\frac{\mathrm{d}v_M}{\mathrm{d}t} = f_M(\boldsymbol{v}) = \frac{E_L - v_M}{\tau_\delta} + \frac{\lambda^2}{\Delta x^2 \tau_\delta}(2v_{M-1} - 2v_M). \tag{35}$$

This allows us to write the Jacobian matrix as

$$\boldsymbol{J} = \begin{pmatrix} \frac{\partial f_{a1}}{\partial a_1} & \cdots & \frac{\partial f_{a1}}{\partial a_K} & \frac{\partial f_{a1}}{\partial v_\sigma} & \frac{\partial f_{a1}}{\partial v_1} & \cdots & \frac{\partial f_{a1}}{\partial v_M} \\ \cdots & \cdots & \cdots & \cdots & \cdots & \cdots & \cdots \\ \frac{\partial f_\sigma}{\partial a_1} & \cdots & \frac{\partial f_\sigma}{\partial a_K} & \frac{\partial f_\sigma}{\partial v_\sigma} & \frac{\partial f_\sigma}{\partial v_1} & \cdots & \frac{\partial f_\sigma}{\partial v_M} \\ \frac{\partial f_1}{\partial a_1} & \cdots & \frac{\partial f_1}{\partial a_K} & \frac{\partial f_1}{\partial v_\sigma} & \frac{\partial f_1}{\partial v_1} & \cdots & \frac{\partial f_1}{\partial f_M} \\ \cdots & \cdots & \cdots & \cdots & \cdots & \cdots & \cdots \\ \frac{\partial f_M}{\partial a_1} & \cdots & \frac{\partial f_M}{\partial a_K} & \frac{\partial f_M}{\partial v_\sigma} & \frac{\partial f_M}{\partial f_1} & \cdots & \frac{\partial f_M}{\partial v_M} \end{pmatrix}, \tag{36}$$

which we will split into four block matrices

$$\boldsymbol{J} = \begin{pmatrix} \mathcal{A} & \mathcal{B} \\ \mathcal{C} & \mathcal{D} \end{pmatrix}, \quad \mathcal{A}_{ij} = \frac{\partial f_{ai}}{\partial a_j}, \quad i, j = 1, ..., K, \quad \mathcal{B}_{ij} = \frac{\partial f_{ai}}{\partial v_j}, \quad i = 1, ..., K, \ j = \sigma, 1, ..., M,$$

$$\mathcal{C}_{ij} = \frac{\partial f_i}{\partial a_j}, \quad i = \sigma, 1, ..., M, \ j = 1, ..., K, \quad \mathcal{D}_{ij} = \frac{\partial f_i}{\partial v_j}, \quad i = \sigma, 1, ..., M, \ j = \sigma, 1, ..., M. \tag{37}$$

For the partial derivatives of f_{ai} we have

$$\frac{\partial f_{ai}}{\partial a_p} = \begin{cases} -\frac{1}{\tau_i(v)}, & i = p \\ 0, & i \neq p \end{cases}, \tag{38}$$

$$\frac{\partial f_{ai}}{\partial v_\sigma} = \frac{1}{\tau_i}\frac{\mathrm{d}a_{i,\infty}}{\mathrm{d}v_\sigma} + (a_{i,\infty} - a_i)\frac{\partial}{\partial v_\sigma}\left(\frac{1}{\tau_i}\right), \tag{39}$$

where $\partial f_{ai}/\partial v_\sigma = \frac{1}{\tau_i}\mathrm{d}a_{i,\infty}/\mathrm{d}v_\sigma$ when evaluated at equilibrium. Since the active variables depend only on the somatic voltage, $\partial f_{ai}/\partial v_k = 0$. In terms of the block matrices, this means that $\mathcal{A}$ is a diagonal matrix with

$$\mathcal{A}_{ii} = -\frac{1}{\tau_i}, \quad i = 1, ..., K, \tag{40}$$

while the matrix $\mathcal{B}$ only has one non-zero column

$$\mathcal{B}_{i\sigma} = \frac{1}{\tau_i}\frac{\mathrm{d}a_{i,\infty}}{\mathrm{d}v_\sigma}, \quad B_{ij} = 0,\ j \neq \sigma. \tag{41}$$

For the somatic voltage equation, we define $\Lambda = \lambda^2/\Delta x^2$ and write the voltage derivatives as

$$\frac{\partial f_\sigma}{\partial v_\sigma} = \frac{\partial f_{\mathrm{S}}}{\partial v_\sigma} - \frac{\sqrt{\Lambda}\rho G_\sigma}{C_\sigma}, \quad \frac{\partial f_\sigma}{\partial v_1} = \frac{\sqrt{\Lambda}\rho G_\sigma}{C_\sigma}, \quad \frac{\partial f_\sigma}{\partial v_k} = 0, \quad k > 1. \tag{42}$$

Turning to the dendritic equations, since the dendrite is passive $\partial f_k/\partial a_i = 0$ for all i, k. For the voltage derivatives

$$\frac{\partial f_1}{\partial v_\sigma} = \frac{\Lambda}{\tau_\delta}, \quad \frac{\partial f_k}{\partial v_\sigma} = 0, \quad k \neq 1, \quad \frac{\partial f_k}{\partial v_j} = \begin{cases} \Lambda/\tau_\delta, & j = k \pm 1,\ k \neq M \\ -(1+2\Lambda)/\tau_\delta, & j = k \\ 0, & \text{otherwise} \end{cases}, \quad \frac{\partial f_M}{\partial v_{M-1}} = 2\Lambda/\tau_\delta, \tag{43}$$

which means that the matrix $\mathcal{C}$ only has one non-zero row

$$\mathcal{C}_{\sigma j} = \frac{\partial f_\sigma}{\partial a_j}, \quad C_{ij} = 0, \quad i \neq \sigma, \tag{44}$$

while $\mathcal{D}$ is a tridiagonal matrix

$$\mathcal{D}_{\sigma\sigma} = \frac{\partial f_{\mathrm{S}}}{\partial v_\sigma} - \frac{\sqrt{\Lambda}\rho G_\sigma}{C_\sigma}, \quad D_{\sigma 1} = \frac{\sqrt{\Lambda}\rho G_\sigma}{C_\sigma},$$
$$\mathcal{D}_{i,i\pm1} = \frac{\Lambda}{\tau_\delta}, \quad \mathcal{D}_{ii} = -\frac{(1+2\Lambda)}{\tau_\delta}, \quad i = 1, ..., M-1, \quad \mathcal{D}_{M,M-1} = \frac{2\Lambda}{\tau_\delta}, \quad \mathcal{D}_{MM} = -\frac{(1+2\Lambda)}{\tau_\delta}. \tag{45}$$

Bogdanov-Takens Bifurcation

At the Bogdanov-Takens bifurcation, the Jacobian has two zero eigenvalues. This means that $\boldsymbol{J}$ has left- and right-eigenvectors which not only satisfy $\boldsymbol{lJ} = \boldsymbol{0}$ and $\boldsymbol{Jr} = \boldsymbol{0}$ but also the orthogonality condition $\boldsymbol{lr} = \boldsymbol{0}$. Denoting th elements of the right-eigenvector as $\boldsymbol{r} = (r_{a1}, ..., r_{aK}, r_\sigma, r_1, ..., r_M)$, the right-eigenvector equations at the BT bifurcation are

$$\begin{gathered}
-\frac{r_{ai}}{\tau_i} + \frac{r_\sigma}{\tau_i}\frac{\mathrm{d}a_{i,\infty}}{\mathrm{d}v_\sigma} = 0, \\
\sum_{i=1}^{K} r_{ai}\frac{\partial f_\sigma}{\partial a_i} + r_\sigma\left(\frac{\partial f_{\mathrm{S}}}{\partial v_\sigma} - \frac{\sqrt{\Lambda}\rho G_\sigma}{C_\sigma}\right) + r_1\frac{\sqrt{\Lambda}\rho G_\sigma}{C_\sigma} = 0, \\
r_{k-1}\frac{\Lambda}{\tau_\delta} - r_k\frac{1+2\Lambda}{\tau_\delta} + r_{k+1}\frac{\Lambda}{\tau_\delta} = 0, \quad k = 1, ..., M-1, \\
2r_{M-1}\frac{\Lambda}{\tau_\delta} - r_M\frac{1+2\Lambda}{\tau_\delta} = 0.
\end{gathered} \tag{46}$$

The aim here is to rewrite all the elements of the eigenvector $\boldsymbol{r}$ in terms of r_σ, and we can immediately see that $r_{ai} = r_\sigma \mathrm{d}a_{i,\infty}/\mathrm{d}v_\sigma$. The dendritic elements meanwhile form a discrete difference equation (DDE)

$$r_{k-1}\Lambda - r_k(1+2\Lambda) + r_{k+1}\Lambda = 0, \quad r_0 = r_\sigma, \quad 2r_{M-1}\Lambda - r_M(1+2\Lambda) = 0, \tag{47}$$

which has the general solution

$$r_k = c_+\mu_+^k + c_-\mu_-^k, \quad \mu_\pm = \frac{1+2\Lambda \pm \sqrt{1+4\Lambda}}{2\Lambda}. \tag{48}$$

Utilising the relations $\mu_+ + \mu_- = (1+2\Lambda)/\Lambda$ and $\mu_+\mu_- = 1$, we can substitute in the boundary conditions to give the specific solution as

$$r_k = r_\sigma \frac{\mu_-^k\mu_+^{M-1}(1-\mu_+^2) - \mu_+^k\mu_-^{M-1}(1-\mu_-^2)}{\mu_+^{M-1}(1-\mu_+^2) - \mu_-^{M-1}(1-\mu_-^2)}, \tag{49}$$

and hence we have shown that all the right-eigenvector elements can be written in terms of r_σ. Meanwhile the left-eigenvector equations are

$$
\begin{gathered}
-\frac{l_{ai}}{\tau_i} + l_\sigma \frac{\partial f_\sigma}{\partial a_i} = 0, \\
\sum_{i=1}^{K} \frac{l_{ai}}{\tau_i} \frac{\mathrm{d}a_{i,\infty}}{\mathrm{d}v_\sigma} + l_\sigma \left(\frac{\partial f_\mathrm{S}}{\partial v_\sigma} - \frac{\sqrt{\Lambda}\rho G_\sigma}{C_\sigma} \right) + l_1 \frac{\partial f_1}{\partial v_\sigma} = 0, \quad l_\sigma \frac{\rho G_\sigma \sqrt{\Lambda}}{C_\mathrm{m}} - l_1 \frac{1+2\Lambda}{\tau_\delta} + l_2 \frac{\Lambda}{\tau_\delta} = 0, \\
l_{k-1} \frac{\Lambda}{\tau_\delta} - l_k \frac{1+2\Lambda}{\tau_\delta} + l_{k+1} \frac{\Lambda}{\tau_\delta} = 0, \quad k = 2, ..., M-2, \\
l_{M-2} \frac{\Lambda}{\tau_\delta} - l_{M-1} \frac{1+2\Lambda}{\tau_\delta} + l_M \frac{2\Lambda}{\tau_\delta} = 0, \quad l_{M-1} \frac{\Lambda}{\tau_\delta} - l_M \frac{1+2\Lambda}{\tau_\delta} = 0,
\end{gathered} \tag{50}
$$

where we can see that $l_{ai} = l_\sigma \tau_i \partial f_\sigma / \partial a_i$. The dendritic elements of $\boldsymbol{l}$ follow the same DDE as before, but with different boundary conditions. This has the solution in terms of l_1

$$
l_k = l_1 \frac{\mu_-^{k-1} \mu_+^{M-2} (1-\mu_+^2) - \mu_+^{k-1} \mu_-^{M-2} (1-\mu_-^2)}{\mu_+^{M-2} (1-\mu_+^2) - \mu_-^{M-2} (1-\mu_-^2)}, \quad k = 1, ..., M-1, \tag{51}
$$

where $\mu_\pm$ is given by (48) and $l_M = l_{M-1}\Lambda/(1+2\Lambda)$. The dendritic elements can be written in terms of l_σ via

$$
l_\sigma \frac{\tau_\delta \rho G_\sigma \sqrt{\Lambda}}{C_\sigma} = l_1 (1 + 2\Lambda - \Lambda S), \quad S = l_{k=2}/l_1, \tag{52}
$$

however ρ is intrinsically linked to g_in, our bifurcation parameter. We can write ρ in terms of the somatic fixed-point voltage v_σ^* from the somatic right-eigenvector equation

$$
\begin{gathered}
\sum_{i=1}^{K} r_{ai} \frac{\partial f_\sigma}{\partial a_i} + r_\sigma \frac{\partial f_\mathrm{S}}{\partial v_\sigma} - \frac{\rho G_\sigma \sqrt{\Lambda}}{C_\sigma} (r_\sigma - r_1) = 0 \\
\rho(v_\sigma^*) = \frac{C_\sigma r_\sigma}{G_\sigma \sqrt{\Lambda} (r_\sigma - r_1)} \left(\frac{\partial f_\mathrm{S}}{\partial v_\sigma} + \sum_{i=1}^{K} \frac{\mathrm{d}a_{i,\infty}}{\mathrm{d}v_\sigma} \frac{\partial f_\sigma}{\partial a_i} \right).
\end{gathered} \tag{53}
$$

This means that each term in our eigenvector product is proportional to $l_\sigma r_\sigma$

$$
\begin{aligned}
\boldsymbol{l}\boldsymbol{r} &= \sum_{i=1}^{K} l_{ai} r_{ai} + l_\sigma r_\sigma + \sum_{k=1}^{M} l_k r_k = 0 \\
&= 1 + \sum_{i=1}^{K} (\tau_i + \alpha_0 \tau_\delta) \frac{\partial f_\sigma}{\partial a_i} \frac{\mathrm{d}a_{i,\infty}}{\mathrm{d}v_\sigma} + \alpha_0 \tau_\delta \frac{\partial f_\mathrm{S}}{\partial v_\sigma},
\end{aligned} \tag{54}
$$

$$
\alpha_0 = \frac{r_\sigma \Sigma_\delta}{(r_\sigma - r_1)(1 + 2\Lambda - \Lambda S)}, \tag{55}
$$

where Σ_δ represents the summation of the dendritic terms,

$$\Sigma_\delta = \sum_{k=1}^{M-1} \frac{\mu_-^{k-1}\mu_+^{M-2}(1-\mu_+^2) - \mu_+^{k-1}\mu_-^{M-2}(1-\mu_-^2)}{\mu_+^{M-2}(1-\mu_+^2) - \mu_-^{M-2}(1-\mu_-^2)} \times \frac{\mu_-^{k}\mu_+^{M-1}(1-\mu_+^2) - \mu_+^{k}\mu_-^{M-1}(1-\mu_-^2)}{\mu_+^{M-1}(1-\mu_+^2) - \mu_-^{M-1}(1-\mu_-^2)}$$
$$+\frac{\Lambda}{1+2\Lambda}\frac{(1-\mu_+^2)-(1-\mu_-^2)}{\mu_+^{M-2}(1-\mu_+^2) - \mu_-^{M-2}(1-\mu_-^2)} \times \frac{\mu_-(1-\mu_+^2)-\mu_+(1-\mu_-^2)}{\mu_+^{M-1}(1-\mu_+^2) - \mu_-^{M-1}(1-\mu_-^2)}. \tag{56}$$

Hence for the *discrete* system, one can numerically solve the eigenvector product equation (54) to obtain v_σ^{BT} and then obtain $G_{\mathrm{in}}^{\mathrm{BT}}$ and $I_{\mathrm{ext}}^{\mathrm{BT}}$ from $I'_\infty = 0$ and $I_\infty = 0$ respectively. However, we can also take the continuum limit to obtain a BT equation for a spatially *continuous* system.

A semi-infinite cable attached to a soma can be analysed by taking the limit $M \to \infty$. Note that we will first consider the spatial step size to be still non-zero, $\Delta x > 0$, and later we will take the continuum limit $\Delta x \to 0$. With an infinite number of compartments, the DDEs for r_k and l_k simply greatly as the new distal boundary conditions are

$$\lim_{k\to\infty} |r_k| < \infty, \quad \lim_{k\to\infty} |l_k| < \infty. \tag{57}$$

From our earlier definition of $\mu_\pm$, for $\Lambda > 0$ $|\mu_+| > 1$ and $|\mu_-| < 1$. This for both l_k and r_k the solutions are

$$r_k = r_\sigma \mu_-^k, \quad l_k = l_1 \mu_-^{k-1}, \quad k = 1, 2, ... \tag{58}$$

This means that the summation of dendritic terms is

$$\Sigma_\delta = \sum_{k=1}^{\infty} \mu_-^{2k-1} = \frac{\mu_-}{1-\mu_-^2}, \tag{59}$$

and hence the factor α_0 is

$$\alpha_0 = \frac{\mu_-}{(1-\mu_-)(1+2\Lambda-\Lambda\mu_-)(1-\mu_-^2)}. \tag{60}$$

Now we take the continuum limit $\Delta x \to 0$ which in this case is equivalent to $\Lambda \to \infty$. α_0 is the only constant that depends on Λ, and has the limit

$$\lim_{\Lambda\to\infty} \alpha_0 = \frac{1}{2}. \tag{61}$$

Substituting α_0 into the BT condition thus gives

$$\sum_{i=1}^{K}\left(\frac{\tau_\delta}{2}+\tau_i\right)\frac{\partial f_\sigma}{\partial a_i}\frac{\mathrm{d}a_{i,\infty}}{\mathrm{d}v_\sigma}+1+\frac{\tau_\delta}{2}\frac{\partial f_\mathrm{S}}{\partial v_\sigma}=0. \tag{62}$$

For the finite cable, after resolving the summation (56), we define $\Delta z=\Delta x/\lambda$. This allows M to be rewritten as $M=\ell/\Delta z$ and $\Lambda=\Delta z^{-2}$. After much algebra, taking the limit $\Delta z\to 0$ gives for α_0

$$\lim_{\Delta z\to 0}\alpha_0=\frac{1}{2}+\frac{\ell}{2\cosh\ell\sinh\ell}. \tag{63}$$

Hopf Bifurcation

At the Hopf bifurcation, there exist right-eigenvectors of the Jacobian $\boldsymbol{J}$ which satisfy $\boldsymbol{J}\boldsymbol{q}=i\omega_\mathrm{H}\boldsymbol{q}$ and $\boldsymbol{J}\overline{\boldsymbol{q}}=-i\omega_\mathrm{H}\overline{\boldsymbol{q}}$. We can use the discretised Jacobian outlined earlier to obtain an expressing for the somatic voltage at the Hopf bifurcation, v_σ^H. For the right eigenvectors we will use the indexing $\boldsymbol{q}=(q_{a1},...,q_{aK},q_\sigma,q_1,...,q_M)$, and hence our right-eigenvector equations are

$$\begin{gathered}-\frac{q_{ai}}{\tau_i}+\frac{q_\sigma}{\tau_i}\frac{\mathrm{d}a_{i,\infty}}{\mathrm{d}v_\sigma}=i\omega_\mathrm{H}q_{ai},\quad \sum_{i=1}^{K}q_{ai}\frac{\partial f_\sigma}{\partial a_i}+q_\sigma\left(\frac{\partial f_\mathrm{S}}{\partial v_\sigma}-\frac{\sqrt{\Lambda}\rho G_\sigma}{C_\sigma}\right)+q_1\frac{\partial f_\sigma}{\partial v_1}=i\omega_\mathrm{H}q_\sigma,\\ q_{k-1}\frac{\Lambda}{\tau_\delta}-q_k\frac{1+2\Lambda}{\tau_\delta}+q_{k+1}\frac{\Lambda}{\tau_\delta}=i\omega_\mathrm{H}q_k,\quad k=1,...,M-1,\quad 2q_{M-1}\frac{\Lambda}{\tau_\delta}-q_M\frac{1+2\Lambda}{\tau_\delta}=i\omega q_M.\end{gathered} \tag{64}$$

We see that the dendritic elements follow a DDE equation similar to the one for the BT bifurcation. We rewrite the DDE and its boundary conditions as

$$\begin{gathered}q_{k-1}\Lambda-q_k(1+2\Lambda+i\omega_\mathrm{H}\tau_\delta)+q_{k+1}\Lambda=0,\quad q_0=q_\sigma,\\ 2q_{M-1}\Lambda-q_M(1+2\Lambda+i\omega_\mathrm{H}\tau_\delta)=0,\end{gathered} \tag{65}$$

where the DDE has a general solution in terms of the bases $\eta_\pm$, a complex analogue of $\mu_\pm$

$$q_k=c_+\eta_+^k+c_-\eta_-^k,\quad \eta_\pm=\frac{1+2\Lambda+i\omega_\mathrm{H}\tau_\delta\pm\sqrt{(1+2\Lambda+i\omega_\mathrm{H}\tau_\delta)^2-4\Lambda^2}}{2\Lambda}. \tag{66}$$

We use the boundary conditions to find $c_\pm$ and hence the specific solution to q_k

$$q_k=q_\sigma\frac{\eta_-^k\eta_+^{M-1}(1-\eta_+^2)-\eta_+^k\eta_-^{M-1}(1-\eta_-^2)}{\eta_+^{M-1}(1-\eta_+^2)-\eta_-^{M-1}(1-\eta_-^2)}. \tag{67}$$

Defining $Q(n) = \eta_+^n(1-\eta_+^2) - \eta_-^n(1-\eta_-^2)$, we can substitute q_1 and q_{ai} into the equation for q_σ to yield

$$\sum_{i=1}^{K} \frac{1 - i\omega_{\mathrm{H}}\tau_i}{1+\omega_{\mathrm{H}}^2\tau_i^2} \frac{\partial f_\sigma}{\partial a_i} \frac{\mathrm{d}a_{i,\infty}}{\mathrm{d}v_\sigma} + \frac{\partial f_{\mathrm{S}}}{\partial v_\sigma} + \frac{\rho G_\sigma \sqrt{\Lambda}}{C_\sigma} \left[\frac{Q(M-2)}{Q(M-1)} - 1 \right] - i\omega_{\mathrm{H}} = 0. \tag{68}$$

Turning back to the eigenvector $\overline{\boldsymbol{q}}$, we obtain the same form of specific solution for the dendritic eigenvector elements, but this time in terms of $\overline{\eta}_\pm$

$$\overline{\eta}_\pm = \frac{1 + 2\Lambda - i\omega_{\mathrm{H}}\tau_\delta \pm \sqrt{(1+2\Lambda - i\omega_{\mathrm{H}}\tau_\delta)^2 - 4\Lambda^2}}{2\Lambda}. \tag{69}$$

This means that the same substitutions into the equation for $\overline{q}_\sigma$ gives

$$\sum_{i=1}^{K} \frac{1 + i\omega_{\mathrm{H}}\tau_i}{1+\omega_{\mathrm{H}}^2\tau_i^2} \frac{\partial f_\sigma}{\partial a_i} \frac{\mathrm{d}a_{i,\infty}}{\mathrm{d}v_\sigma} + \frac{\partial f_{\mathrm{S}}}{\partial v_\sigma} + \frac{\rho G_\sigma \sqrt{\Lambda}}{C_\sigma} \left[\frac{\overline{Q}(M-2)}{\overline{Q}(M-1)} - 1 \right] + i\omega_{\mathrm{H}} = 0, \tag{70}$$

where $\overline{Q}(n)$ has the same definition as Q, but in terms of $\overline{\eta}_\pm$.

For the semi-infinite dendrite first we take $M \to \infty$, which has the effect of simplifying the specific solution of the DDEs to

$$q_k = q_\sigma \eta_-^k, \quad \overline{q}_k = q_\sigma \overline{\eta}_-^k. \tag{71}$$

The equations for q_σ and $\overline{q}_\sigma$ are hence simplified to

$$\sum_{i=1}^{K} \frac{1 - i\omega_{\mathrm{H}}\tau_i}{1+\omega_{\mathrm{H}}^2\tau_i^2} \frac{\partial f_\sigma}{\partial a_i} \frac{\mathrm{d}a_{i,\infty}}{\mathrm{d}v_\sigma} + \frac{\partial f_{\mathrm{S}}}{\partial v_\sigma} + \frac{\rho G_\sigma \sqrt{\Lambda}}{C_\sigma} (\eta_- - 1) - i\omega_{\mathrm{H}} = 0, \tag{72}$$

$$\sum_{i=1}^{K} \frac{1 + i\omega_{\mathrm{H}}\tau_i}{1+\omega_{\mathrm{H}}^2\tau_i^2} \frac{\partial f_\sigma}{\partial a_i} \frac{\mathrm{d}a_{i,\infty}}{\mathrm{d}v_\sigma} + \frac{\partial f_{\mathrm{S}}}{\partial v_\sigma} + \frac{\rho G_\sigma \sqrt{\Lambda}}{C_\sigma} (\overline{\eta}_- - 1) + i\omega_{\mathrm{H}} = 0. \tag{73}$$

Now we take the continuum limit ($\Lambda \to \infty$) of the only term that varies with Λ

$$\lim_{\Lambda\to\infty} \sqrt{\Lambda}(\eta_- - 1) = -\frac{\sqrt{4\Lambda + 4i\omega_{\mathrm{H}}\tau_\delta\Lambda}}{2\sqrt{\Lambda}} = -\sqrt{1 + i\omega_{\mathrm{H}}\tau_\delta} = -\gamma(\omega_{\mathrm{H}}). \tag{74}$$

We similarly find that

$$\lim_{\Lambda\to\infty} \sqrt{\Lambda}(\overline{\eta} - 1) = -\sqrt{1 - i\omega_{\mathrm{H}}\tau_\delta} = -\gamma(-\omega_{\mathrm{H}}). \tag{75}$$

It can be shown that $\gamma(\omega_{\mathrm{H}})$ and $\gamma(-\omega_{\mathrm{H}})$ are complex conjugates with a sum and difference given by

$$\gamma(\omega_{\mathrm{H}}) + \gamma(-\omega_{\mathrm{H}}) := s_\gamma(\omega_{\mathrm{H}}) = \sqrt{2 + 2\sqrt{1 + \omega_{\mathrm{H}}^2 \tau_\delta^2}}, \tag{76}$$

$$\gamma(\omega_{\mathrm{H}}) - \gamma(-\omega_{\mathrm{H}}) := i d_\gamma(\omega_{\mathrm{H}}) = i\,\mathrm{sgn}(\omega_{\mathrm{H}})\sqrt{-2 + 2\sqrt{1 + \omega_{\mathrm{H}}^2 \tau_\delta^2}}. \tag{77}$$

This means that summing (72) and (73) in the continuum limit gives the real-valued equation

$$\sum_{i=1}^{K} \frac{1}{1 + \omega_{\mathrm{H}}^2 \tau_i^2} \frac{\partial f_\sigma}{\partial a_i} \frac{\mathrm{d}a_{i,\infty}}{\mathrm{d}v_\sigma} + \frac{\partial f_{\mathrm{S}}}{\partial v_\sigma} - \frac{\rho G_\sigma}{2C_\sigma} s_\gamma(\omega_{\mathrm{H}}) = 0, \tag{78}$$

while subtracting (72) from (73) gives an equation in terms of the imaginary part

$$\sum_{i=1}^{K} \frac{\tau_i}{1 + \omega_{\mathrm{H}}^2 \tau_i^2} \frac{\partial f_\sigma}{\partial a_i} \frac{\mathrm{d}a_{i,\infty}}{\mathrm{d}v_\sigma} + \frac{\rho G_\sigma}{2C_\sigma} \frac{d_\gamma(\omega_{\mathrm{H}})}{\omega_{\mathrm{H}}} + 1 = 0. \tag{79}$$

These nonlinear equations can be solved simultaneously to find ω_{H} and v_σ^{H}.

To find the finite continuum limit solution for the Hopf bifurcation, we first find the continuum limits of $\sqrt{\Lambda}[Q(M-2)/Q(M-1) - 1]$ and $\sqrt{\Lambda}[\overline{Q}(M-2)/\overline{Q}(M-1) - 1]$ in (68) and (70) by substituting $\Lambda = \Delta z^{-2}$ and $M = l/\Delta z$ as in the BT section. After doing so, the first Hopf equation (68) becomes

$$\sum_{i=1}^{K} \frac{1 - i\omega_{\mathrm{H}}\tau_i}{1 + \omega_{\mathrm{H}}^2 \tau_i^2} \frac{\partial f_\sigma}{\partial a_i} \frac{\mathrm{d}a_{i,\infty}}{\mathrm{d}v_\sigma} + \frac{\partial f_{\mathrm{S}}}{\partial v_\sigma} - \frac{\rho G_\sigma}{C_\sigma} \gamma(\omega_{\mathrm{H}}) \tanh[l\gamma(\omega_{\mathrm{H}})] - i\omega_{\mathrm{H}} = 0, \tag{80}$$

and the continuum-limit of the second Hopf equation (70) is

$$\sum_{i=1}^{K} \frac{1 + i\omega_{\mathrm{H}}\tau_i}{1 + \omega_{\mathrm{H}}^2 \tau_i^2} \frac{\partial f_\sigma}{\partial a_i} \frac{\mathrm{d}a_{i,\infty}}{\mathrm{d}v_\sigma} + \frac{\partial f_{\mathrm{S}}}{\partial v_\sigma} - \frac{\rho G_\sigma}{C_\sigma} \gamma(-\omega_{\mathrm{H}}) \tanh[l\gamma(-\omega_{\mathrm{H}})] + i\omega_{\mathrm{H}} = 0. \tag{81}$$

Now when we sum and difference (80) and (81) we get equations for the real and imaginary parts

$$\sum_{i=1}^{K} \frac{1}{1 + \omega_{\mathrm{H}}^2 \tau_i^2} \frac{\partial f_\sigma}{\partial a_i} \frac{\mathrm{d}a_{i,\infty}}{\partial v_\sigma} + \frac{\partial f_{\mathrm{S}}}{\partial v_\sigma} - \frac{\rho G_\sigma}{2C_\sigma} \frac{s_\gamma \sinh(l s_\gamma) - d_\gamma \sin(l d_\gamma)}{\cosh(l s_\gamma) + \cos(l d_\gamma)} = 0, \tag{82}$$

$$\sum_{i=1}^{K} \frac{\tau_i}{1 + \omega_{\mathrm{H}}^2 \tau_i^2} \frac{\partial f_\sigma}{\partial a_i} \frac{\mathrm{d}a_{i,\infty}}{\mathrm{d}v_\sigma} + \frac{\rho G_\sigma}{2C_\sigma} \frac{d_\gamma \sinh(l s_\gamma) + s_\gamma \sin(l d_\gamma)}{\omega_{\mathrm{H}}[\cosh(l s_\gamma) + \cos(l d_\gamma)]} + 1 = 0. \tag{83}$$

These two nonlinear equations must be solved simultaneously. In this case, we used a trust-region method implemented by the NLsolve.jl package [87].

Criticality of the Hopf Bifurcation

The criticality of the Hopf bifurcation can be obtained from the first Lyapunov coefficient of the equilibrium that undergoes the Hopf bifurcation

$$\mathcal{L}_1 = \frac{1}{2\omega_{\mathrm{H}}}\mathrm{Re}\left\{\overline{\boldsymbol{p}}\boldsymbol{C}(\boldsymbol{q},\boldsymbol{q},\overline{\boldsymbol{q}}) - 2\overline{\boldsymbol{p}}\boldsymbol{B}[\boldsymbol{q},\boldsymbol{J}^{-1}\boldsymbol{B}(\boldsymbol{q},\overline{\boldsymbol{q}})] + \overline{\boldsymbol{p}}\boldsymbol{B}[\overline{\boldsymbol{q}},(2i\omega_{\mathrm{H}}\boldsymbol{I}-\boldsymbol{J})^{-1}\boldsymbol{B}(\boldsymbol{q},\boldsymbol{q})]\right\}, \tag{84}$$

where $\boldsymbol{q}$ is the right-eigenvector of $\boldsymbol{J}$ at the Hopf bifurcation found earlier, $\boldsymbol{p}$ is the left-eigenvector of $\boldsymbol{J}$, and $\boldsymbol{B}$ and $\boldsymbol{C}$ are the second and third order tensors of the system. When $\mathcal{L}_1 < 0$, the Hopf bifurcation is supercritical, while when $\mathcal{L}_1 > 0$ it is subcritical. The left-eigenvectors satisfy $\boldsymbol{p}\boldsymbol{J} = -i\omega_{\mathrm{H}}\boldsymbol{p}$ and $\overline{\boldsymbol{p}}\boldsymbol{J} = i\omega_{\mathrm{H}}\overline{\boldsymbol{p}}$ while the ith element of each evaluated tensor is

$$B_i(\boldsymbol{x},\boldsymbol{y}) = \sum_{j,k}\frac{\partial^2 f_i}{\partial\xi_j\partial\xi_k}x_j y_k, \quad C_i(\boldsymbol{x},\boldsymbol{y},\boldsymbol{z}) = \sum_{j,k,l}\frac{\partial^3 f_i}{\partial\xi_j\partial\xi_k\partial\xi_l}x_j y_k z_l. \tag{85}$$

Due to the linearity of the passive dendrite, the dendritic terms of B_i and C_i will be zero. Thus, we only need calculate the $K+1$ terms for each active value and the somatic voltage, which use the eigenvector elements $q_i, ..., q_K, q_\sigma$. Using the normalisation $\overline{\boldsymbol{p}}\boldsymbol{q} = 1$, we can write all the eigenvector elements of $\boldsymbol{p}$ and $\boldsymbol{q}$ in terms of q_σ in the continuum limit

$$\overline{p}_\sigma = \frac{q_\sigma}{\kappa}, \quad \kappa = \sum_{i=1}^{K}\frac{\tau_i}{(1+i\omega_{\mathrm{H}}\tau_i)^2}\frac{\partial f_\sigma}{\partial a_i}\frac{\mathrm{d}a_{i,\infty}}{\mathrm{d}v_\sigma} + 1 + \frac{\tau_\delta\rho g_\sigma}{C_\sigma}\frac{(e^{2\ell\gamma}-e^{-2\ell\gamma}+4\ell\gamma)}{2\gamma(e^{\ell\gamma}+e^{-\ell\gamma})^2}, \tag{86}$$

$$\overline{p}_{ai} = \frac{\overline{p}_\sigma\tau_i}{1+i\omega_{\mathrm{H}}\tau_i}\frac{\partial f_\sigma}{\partial a_i}, \quad q_{ai} = \frac{q_\sigma}{1+i\omega_{\mathrm{H}}\tau_i}\frac{\mathrm{d}a_{i,\infty}}{\mathrm{d}v_\sigma}. \tag{87}$$

For the terms involving inverse matrices, elements required for calculation of $\boldsymbol{B}$ also have continuum limits. Denoting $\boldsymbol{u} = \boldsymbol{J}^{-1}\boldsymbol{B}(\boldsymbol{q},\overline{\boldsymbol{q}})$, we require the elements $u_{a1}, ..., u_{aK}, u_\sigma$. Since only the first $K+1$ elements of $\boldsymbol{B}$ are non-zero, this means only the calculation of $(K+1)\times(K+1)$ elements of $\boldsymbol{J}^{-1}$ is necessary. The block structure of $\boldsymbol{J}$ defined earlier (36) means that its inverse elements can be found in terms of the blocks

$$\boldsymbol{J} = \begin{pmatrix}\mathcal{A} & \mathcal{B}\\ \mathcal{C} & \mathcal{D}\end{pmatrix}, \quad \boldsymbol{J}^{-1} = \begin{pmatrix}\mathcal{A}^{-1}+\mathcal{A}^{-1}\mathcal{B}\mathcal{S}^{-1}\mathcal{C}\mathcal{A}^{-1} & -\mathcal{A}^{-1}\mathcal{B}\mathcal{S}^{-1}\\ -\mathcal{S}^{-1}\mathcal{C}\mathcal{A}^{-1} & \mathcal{S}^{-1}\end{pmatrix}. \tag{88}$$

Here $\mathcal{S} = \mathcal{D} - \mathcal{C}\mathcal{A}^{-1}\mathcal{B}$ is the Schur complement. Using this approach, the upper-left $(K+1) \times (K+1)$ quadrant of $\boldsymbol{J}^{-1}$ can be found as

$$[\boldsymbol{J}^{-1}]_{ij} = \begin{cases} -\tau_i + [\mathcal{S}^{-1}]_{11}\tau_i \frac{\mathrm{d}a_{i,\infty}}{\mathrm{d}v_\sigma}\frac{\partial f_\sigma}{\partial a_i}, \quad i = j, \quad i,j \neq \sigma \\ [\mathcal{S}^{-1}]_{11}\tau_j \frac{\mathrm{d}a_{i,\infty}}{\mathrm{d}v_\sigma}\frac{\partial f_\sigma}{\partial a_j}, \quad i \neq j, \quad i,j \neq \sigma \\ [\mathcal{S}^{-1}]_{11}\frac{\mathrm{d}a_{i,\infty}}{\mathrm{d}v_\sigma}, \quad i \neq \sigma, \quad j = \sigma \\ [\mathcal{S}^{-1}]_{11}\tau_j \frac{\partial f_\sigma}{\partial a_j}, \quad i = \sigma, \quad j \neq \sigma \\ [\mathcal{S}^{-1}]_{11}, \quad i = j = \sigma \end{cases}, \tag{89}$$

where in the continuum limit $[\mathcal{S}^{-1}]_{11}$ is the inverse of the total derivative of the somatic voltage equation with respect to v_σ

$$[\mathcal{S}^{-1}]_{11} = \left(\frac{\partial f_{\mathrm{S}}}{\partial v_\sigma} + \sum_{i=1}^{K} \tau_i \frac{\partial f_{ai}}{\partial v_\sigma}\frac{\partial f_\sigma}{\partial a_i} - \frac{\rho G_\sigma}{C_\sigma}\tanh \ell\right)^{-1}. \tag{90}$$

The $(K+1) \times (K+1)$ upper-left quadrant can be calculated for the inverse of $\tilde{\boldsymbol{J}} = \boldsymbol{J} - 2i\omega_{\mathrm{H}}\boldsymbol{I}$ in a similar manner, yielding

$$[\tilde{\boldsymbol{J}}^{-1}]_{ij} = \begin{cases} -\tilde{\tau}_i + [\tilde{\mathcal{S}}^{-1}]_{11}\frac{\tilde{\tau}_i^2}{\tau_i}\frac{\mathrm{d}a_{i,\infty}}{\mathrm{d}v_\sigma}\frac{\partial f_\sigma}{\partial a_i}, \quad i = j, \quad i,j \neq \sigma \\ [\tilde{\mathcal{S}}^{-1}]_{11}\frac{\tilde{\tau}_i\tilde{\tau}_j}{\tau_i}\frac{\mathrm{d}a_{i,\infty}}{\mathrm{d}v_\sigma}\frac{\partial f_\sigma}{\partial a_j}, \quad i \neq j, \quad i,j \neq \sigma \\ [\tilde{\mathcal{S}}^{-1}]_{11}\frac{\tilde{\tau}_i}{\tau_i}\frac{\mathrm{d}a_{i,\infty}}{\mathrm{d}v_\sigma}, \quad i \neq \sigma, \quad j = \sigma \\ [\tilde{\mathcal{S}}^{-1}]_{11}\tilde{\tau}_j \frac{\partial f_\sigma}{\partial a_j}, \quad i = \sigma, \quad j \neq \sigma \\ [\tilde{\mathcal{S}}^{-1}]_{11}, \quad i = j = \sigma \end{cases}, \tag{91}$$

where $\tilde{\tau}_i = \tau_i/(1 + 2i\omega_{\mathrm{H}}\tau_i)$ and

$$[\tilde{\mathcal{S}}^{-1}]_{11} = \left\{\frac{\partial f_{\mathrm{S}}}{\partial v_\sigma} + \sum_{i=1}^{K} \tilde{\tau}_i \frac{\partial f_\sigma}{\partial a_i}\frac{\partial f_{ai}}{\partial v_\sigma} - 2i\omega_{\mathrm{H}} - \frac{\rho G_\sigma}{C_\sigma}\gamma(2\omega_{\mathrm{H}})\tanh[\ell\gamma(2\omega_{\mathrm{H}})]\right\}^{-1}, \tag{92}$$

with γ having the same form as before. This provides us with all the information required to calculate the criticality of a Hopf bifurcation in the continuum limit.

Dendritic Current Input

Moving the external current input to an arbitrary dendritic location x_{in} changes the cable equation to

$$\tau_\delta \frac{\partial v_\delta}{\partial t} = E_L - v_\delta + \lambda^2 \frac{\partial^2 v_\delta}{\partial x^2} + \frac{\lambda I_{\text{ext}}}{\rho G_\sigma} \delta(x - x_{\text{in}}), \tag{93}$$

while the somatic equation remains as in (13) with $I_{\text{ext}} = 0$ at the soma. Setting all time derivatives to zero, the dendritic equilibrium voltage for the semi-infinite dendrite satisfies

$$v_\delta^*(x) = E_L + (v_\sigma^* - E_L)e^{-x/\lambda} + [e^{-|x-x_{\text{in}}|/\lambda} - e^{-|x-x_{\text{in}}|/\lambda}], \tag{94}$$

which means that the somatic fixed point potential is found by solving

$$I_\infty(v_\sigma) = C_\sigma f_{\text{S}}(\boldsymbol{a}_\infty(v_\sigma), v_\sigma) + \rho G_\sigma (E_L - v_\sigma) + I_{\text{ext}} e^{-x_{\text{in}}/\lambda} = 0. \tag{95}$$

Meanwhile for finite dendrite, the dendritic equilibrium voltage with $z = x/\lambda$ obeys

$$\begin{aligned} v_\delta^*(x) = E_L + (v_\sigma - E_L)\cosh z + \left\{ \frac{I_{\text{ext}}}{\rho G_\sigma} \frac{\cosh(\ell - z)}{\cosh \ell} - (v_\sigma - E_L)\tanh \ell \right\} \sinh z \\ -\theta(z - z_{\text{in}}) \frac{I_{\text{ext}}}{\rho G_\sigma} \sinh(z - z_{\text{in}}), \end{aligned} \tag{96}$$

which when substituted into the somatic boundary condition yields

$$I_\infty(v_\sigma) = C_\sigma f_{\text{S}}(\boldsymbol{a}_\infty(v_\sigma), v_\sigma) + \rho G_\sigma \tanh \ell (E_L - v_\sigma) + I_{\text{ext}} \frac{\cosh(\ell - z_{\text{in}})}{\cosh \ell} = 0. \tag{97}$$

In both the semi-infinite and finite models, the only term of the steady-state current equations affected by the spatial separation between the soma at point of current injection, x_{in}, is the external current term. The steady-state current equations converge to the somatically driven case when $x_{\text{in}} = 0$ as expected.

This means that for the saddle-node and cusp bifurcations, differentiating (95) or (97) with respect to v_σ removes all dependence on the location of synaptic input. Therefore, for the same values of τ_δ and ρ, v_σ^{SN} does not vary with x_{in} and has the same value as when external current is applied at the soma. Similarly, for the same τ_δ, ρ^{C} and v^{C} do not depend on x_{in}. $I_{\text{ext}}^{\text{SN}}$ and $I_{\text{ext}}^{\text{C}}$ are the only parameters altered by the spatial location.

For the BT and Hopf bifurcations, we must discretise the cable equation and perform the method of lines. However, since the external dendritic drive does not depend on any of the system variables, the discretised Jacobian $\boldsymbol{J}$ will not depend x_{in} and will thus be identical to the somatically driven scenario. Since the bifurcation parameters for the BT and Hopf bifurcations are derived from the eigenvectors of $\boldsymbol{J}$, this means that they have values which do not vary with x_{in}. Only I_{ext} varies with x_{in}, as was the case for the saddle-node and cusp bifurcations.

Estimation of Global Bifurcations

Global bifurcations govern many spiking onset types and spiking onset transitions, but cannot be directly calculated from the properties of fixed points. Therefore one must use numerical continuation methods [88, 89] and/or numerical simulation in order to estimate the locations of global bifurcations. For simplicity of implementation and to be understood by a wider audience, here we outline how simulation can be used to estimate the location of two global bifurcations of interest.

Homoclinic Bifurcation

At a homoclinic (HOM) bifurcation, a homoclinic orbit is formed at a saddle. If this orbit is stable, then it forms a spiking cycle. HOM onset is class I but its f–I curve typically grows very rapidly in comparison to SNIC onset [40]. Since the HOM bifurcation does not involve changes to the stability of fixed points, a stable homoclinic orbit typically coexists with a stable fixed point. This means that HOM onset allows bistability between quiescence and regular spiking. If the homoclinic orbit contains a single fixed point (other than the saddle), then it is termed a small-HOM (sHOM) bifurcation, while if orbit contains all three fixed points, it is a big-HOM (bHOM) bifurcation.

Using I_{ext} as a bifurcation parameter, if a stable HOM bifurcation exists then it often precedes a SN bifurcation, $I_{\text{ext}}^{\text{HOM}} < I_{\text{ext}}^{\text{SN}}$. Thus we can find the HOM bifurcation as follows:

1. At a given $G_{\text{in}} < G_{\text{in}}^{\text{BT}}$, find the onset current $I_{\text{ext}}^{\text{on}}$ for regular spiking.
2. If $I_{\text{ext}}^{\text{on}} > I_{\text{ext}}^{\text{SN}}$ there is no bistability, and spiking onset occurs via a SNIC bifurcation.
3. If $I_{\text{ext}}^{\text{on}} < I_{\text{ext}}^{\text{SN}}$, bistability exists and a HOM bifurcation is a candidate for the onset type.
4. Repeat this process at various G_{in} to obtain an estimate of the HOM bifurcation for the input conductance range of interest.

We specify $G_{\text{in}} < G_{\text{in}}^{\text{BT}}$ in step (1) here to avoid the presence of Hopf bifurcations. In step (3), we can only conclude that a HOM bifurcation is a candidate for the onset type because the true onset bifurcation may be a fold of limit cycles (FLC) that shortly precedes a subcritical HOM bifurcation [41, 13]. Nevertheless, this procedure forms the basis of finding the switch between SNIC and HOM onset.

Saddle-Node-Loop (SNL) Bifurcation

A saddle-node-loop (SNL) bifurcation is where a saddle-node and HOM bifurcation meet and has codimension two. With $(G_{\text{in}}, I_{\text{ext}})$ as bifurcation parameters, we can therefore switch between SNIC and HOM onset by varying G_{in} around this bifurcation. The SNL bifurcation can be estimated via the following bisection procedure:

1. Find input conductances $G_{\text{in}}^{\text{SNIC}}$ and $G_{\text{in}}^{\text{HOM}}$ for which spiking onset occurs via SNIC and (candidate) HOM bifurcations respectively.
2. Choose a new input conductance between these two points $G_{\text{in}}^{\text{test}} = \frac{1}{2}(G_{\text{in}}^{\text{SNIC}} + G_{\text{in}}^{\text{HOM}})$ and find its onset current $I_{\text{ext}}^{\text{test}}$.
3. Using the procedure for evaluating whether the onset is due to a HOM bifurcation, evaluate the candidate bifurcation type for onset at $G_{\text{in}}^{\text{test}}$.
4. Repeat step (1) with $G_{\text{in}}^{\text{test}}$ replacing the bound of its candidate bifurcation type.
5. Stop after a given number of steps or after $G_{\text{in}}^{\text{test}}$ converges. The final value of $G_{\text{in}}^{\text{test}}$ gives an estimate of $G_{\text{in}}^{\text{SNL}}$.

References

1. E. Marder and D. Bucher, "Central pattern generators and the control of rhythmic movements," *Current biology*, vol. 11, no. 23, pp. R986–R996, 2001.
2. S. Hürkey, N. Niemeyer, J.-H. Schleimer, S. Ryglewski, S. Schreiber, and C. Duch, "Insect asynchronous flight requires neural circuit de-synchronization by electrical synapses," *bioRxiv*, 2022.
3. H. Bergman and G. Deuschl, "Pathophysiology of Parkinson's disease: From clinical neurology to basic neuroscience and back," *Movement Disorders*, vol. 17, pp. S28–S40, Mar. 2002.

4. P. J. Uhlhaas and W. Singer, "Abnormal neural oscillations and synchrony in schizophrenia," *Nature Reviews Neuroscience*, vol. 11, no. 2, pp. 100–113, 2010.

5. P. Jiruska, M. De Curtis, J. G. Jefferys, C. A. Schevon, S. J. Schiff, and K. Schindler, "Synchronization and desynchronization in epilepsy: controversies and hypotheses," *The Journal of physiology*, vol. 591, no. 4, pp. 787–797, 2013.

6. I. Al-Darabsah and S. A. Campbell, "M-current induced bogdanov–takens bifurcation and switching of neuron excitability class," *The Journal of Mathematical Neuroscience*, vol. 11, no. 1, pp. 1–26, 2021.

7. J. Hesse, J.-H. Schleimer, N. Maier, D. Schmitz, and S. Schreiber, "Temperature elevations can induce switches to homoclinic action potentials that alter neural encoding and synchronization," *Nature Communications*, vol. 13, no. 1, pp. 1–12, 2022.

8. A. L. Hodgkin, "The local electric changes associated with repetitive action in a non-medullated axon," *The Journal of physiology*, vol. 107, no. 2, p. 165, 1948.

9. E. M. Izhikevich, "Synchronization," in *Dynamical systems in neuroscience*, ch. 10, pp. 443–505, MIT press, 2007.

10. J. Hesse, J.-H. Schleimer, and S. Schreiber, "Qualitative changes in phase-response curve and synchronization at the saddle-node-loop bifurcation," *Physical Review E*, vol. 95, no. 5, p. 052203, 2017.

11. K. M. Stiefel, B. S. Gutkin, and T. J. Sejnowski, "Cholinergic neuromodulation changes phase response curve shape and type in cortical pyramidal neurons," *PloS one*, vol. 3, no. 12, p. e3947, 2008.

12. S. A. Prescott, Y. De Koninck, and T. J. Sejnowski, "Biophysical basis for three distinct dynamical mechanisms of action potential initiation," *PLoS computational biology*, vol. 4, no. 10, p. e1000198, 2008.

13. C. Kirst, J. Ammer, F. Felmy, A. Herz, and M. Stemmler, "Gaba regulates resonance and spike rate encoding via a universal mechanism that underlies the modulation of action potential generation," *bioRxiv*, p. 206581, 2017.

14. S. A. Contreras, J.-H. Schleimer, A. T. Gulledge, and S. Schreiber, "Activity-mediated accumulation of potassium induces a switch in firing pattern and neuronal excitability type," *PLoS Computational Biology*, vol. 17, no. 5, p. e1008510, 2021.

15. Z. F. Mainen and T. J. Sejnowski, "Influence of dendritic structure on firing pattern in model neocortical neurons," *Nature*, vol. 382, no. 6589, pp. 363–366, 1996.

16. G. Eyal, H. D. Mansvelder, C. P. de Kock, and I. Segev, "Dendrites impact the encoding capabilities of the axon," *Journal of Neuroscience*, vol. 34, no. 24, pp. 8063–8071, 2014.

17. L. Tiroshi and J. A. Goldberg, "Population dynamics and entrainment of basal ganglia pacemakers are shaped by their dendritic arbors," *PLOS Computational Biology*, vol. 15, no. 2, p. e1006782, 2019.

18. D. Beniaguev, S. Shapira, I. Segev, and M. London, "Multiple synaptic contacts combined with dendritic filtering enhance spatio-temporal pattern recognition capabilities of single neurons," *bioRxiv*, 2022.

19. B. Ermentrout, "Type i membranes, phase resetting curves, and synchrony," *Neural computation*, vol. 8, no. 5, pp. 979–1001, 1996.

20. J.-n. Teramae and D. Tanaka, "Robustness of the noise-induced phase synchronization in a general class of limit cycle oscillators," *Physical review letters*, vol. 93, no. 20, p. 204103, 2004.

21. T.-W. Ko and G. B. Ermentrout, "Phase-response curves of coupled oscillators," *Physical Review E*, vol. 79, no. 1, p. 016211, 2009.

22. A. Larkman and A. Mason, "Correlations between morphology and electrophysiology of pyramidal neurons in slices of rat visual cortex. i. establishment of cell classes," *Journal of Neuroscience*, vol. 10, no. 5, pp. 1407–1414, 1990.

23. H. Mohan, M. B. Verhoog, K. K. Doreswamy, G. Eyal, R. Aardse, B. N. Lodder, N. A. Goriounova, B. Asamoah, A. C. B. Brakspear, C. Groot, *et al.*, "Dendritic and axonal architecture of individual pyramidal neurons across layers of adult human neocortex," *Cerebral Cortex*, vol. 25, no. 12, pp. 4839–4853, 2015.

24. K. I. Van Aerde and D. Feldmeyer, "Morphological and physiological characterization of pyramidal neuron subtypes in rat medial prefrontal cortex," *Cerebral cortex*, vol. 25, no. 3, pp. 788–805, 2015.

25. U. Pereira, P. Coullet, and E. Tirapegui, "The bogdanov–takens normal form: a minimal model for single neuron dynamics," *Entropy*, vol. 17, no. 12, pp. 7859–7874, 2015.

26. W. Rall, "Membrane potential transients and membrane time constant of motoneurons," *Experimental neurology*, vol. 2, no. 5, pp. 503–532, 1960.

27. H. C. Tuckwell, *Introduction to theoretical neurobiology: linear cable theory and dendritic structure*, vol. 1. Cambridge University Press, 1988.

28. W. Rall and J. Rinzel, "Branch input resistance and steady attenuation for input to one branch of a dendritic neuron model," *Biophysical journal*, vol. 13, no. 7, pp. 648–688, 1973.

29. W. Rall, "Core conductor theory and cable properties of neurons," in *Comprehensive Physiology*, ch. 3, pp. 39–97, Wiley Online Library, 2011.

30. G. Eyal, M. B. Verhoog, G. Testa-Silva, Y. Deitcher, J. C. Lodder, R. Benavides-Piccione, J. Morales, J. DeFelipe, C. P. de Kock, H. D. Mansvelder, *et al.*, "Unique membrane properties and enhanced signal processing in human neocortical neurons," *Elife*, vol. 5, p. e16553, 2016.

31. L. Beaulieu-Laroche, E. H. Toloza, M.-S. Van der Goes, M. Lafourcade, D. Barnagian, Z. M. Williams, E. N. Eskandar, M. P. Frosch, S. S. Cash, and M. T. Harnett, "Enhanced dendritic compartmentalization in human cortical neurons," *Cell*, vol. 175, no. 3, pp. 643–651, 2018.

32. L. Bindman, T. Meyer, and C. Prince, "Comparison of the electrical properties of neocortical neurones in slices in vitro and in the anaesthetized rat," *Experimental brain research*, vol. 69, no. 3, pp. 489–496, 1988.

33. D. Paré, E. Shink, H. Gaudreau, A. Destexhe, and E. J. Lang, "Impact of spontaneous synaptic activity on the resting properties of cat neocortical pyramidal neurons in vivo," *Journal of neurophysiology*, vol. 79, no. 3, pp. 1450–1460, 1998.

34. A. Destexhe and D. Paré, "Impact of network activity on the integrative properties of neocortical pyramidal neurons in vivo," *Journal of neurophysiology*, vol. 81, no. 4, pp. 1531–1547, 1999.

35. C. Morris and H. Lecar, "Voltage oscillations in the barnacle giant muscle fiber," *Biophysical journal*, vol. 35, no. 1, pp. 193–213, 1981.

36. K. Tsumoto, H. Kitajima, T. Yoshinaga, K. Aihara, and H. Kawakami, "Bifurcations in morris–lecar neuron model," *Neurocomputing*, vol. 69, no. 4-6, pp. 293–316, 2006.

37. C. Liu, X. Liu, and S. Liu, "Bifurcation analysis of a morris–lecar neuron model," *Biological cybernetics*, vol. 108, no. 1, pp. 75–84, 2014.

38. S. Schecter, "The saddle-node separatrix-loop bifurcation," *SIAM journal on mathematical analysis*, vol. 18, no. 4, pp. 1142–1156, 1987.

39. J. Guckenheimer and J. Labouriau, "Bifurcation of the hodgkin and huxley equations: a new twist," *Bulletin of Mathematical Biology*, vol. 55, no. 5, pp. 937–952, 1993.

40. E. M. Izhikevich, *Bifurcations*. MIT press, 2007.

41. P. De Maesschalck and M. Wechselberger, "Neural excitability and singular bifurcations," *The Journal of Mathematical Neuroscience (JMN)*, vol. 5, no. 1, pp. 1–32, 2015.

42. C. Kirst, "Synchronization, neuronal excitability, and information flow in networks of neuronal oscillators," ch. 10, Georg-August-Universität Göttingen, 2011.

43. E. Phoka, H. Cuntz, A. Roth, and M. Häusser, "A new approach for determining phase response curves reveals that purkinje cells can act as perfect integrators," *PLoS computational biology*, vol. 6, no. 4, p. e1000768, 2010.

44. S. Wang, M. M. Musharoff, C. C. Canavier, and S. Gasparini, "Hippocampal ca1 pyramidal neurons exhibit type 1 phase-response curves and type 1 excitability," *Journal of neurophysiology*, vol. 109, no. 11, pp. 2757–2766, 2013.

45. D. Hansel, G. Mato, and C. Meunier, "Synchrony in excitatory neural networks," *Neural computation*, vol. 7, no. 2, pp. 307–337, 1995.

46. E. Brown, J. Moehlis, and P. Holmes, "On the phase reduction and response dynamics of neural oscillator populations," *Neural computation*, vol. 16, no. 4, pp. 673–715, 2004.

47. J.-H. Schleimer and S. Schreiber, "Phase-response curves of ion channel gating kinetics," *Mathematical Methods in the Applied Sciences*, vol. 41, no. 18, pp. 8844–8858, 2018.

48. P. Vetter, A. Roth, and M. Häusser, "Propagation of action potentials in dendrites depends on dendritic morphology," *Journal of neurophysiology*, vol. 85, no. 2, pp. 926–937, 2001.

49. G. A. Ascoli, D. E. Donohue, and M. Halavi, "Neuromorpho. org: a central resource for neuronal morphologies," *Journal of Neuroscience*, vol. 27, no. 35, pp. 9247–9251, 2007.

50. O. Amsalem, G. Eyal, N. Rogozinski, M. Gevaert, P. Kumbhar, F. Schürmann, and I. Segev, "An efficient analytical reduction of detailed nonlinear neuron models," *Nature communications*, vol. 11, no. 1, pp. 1–13, 2020.

51. P. Ashwin, C. Bick, and O. Burylko, "Identical phase oscillator networks: Bifurcations, symmetry and reversibility for generalized coupling," *Frontiers in Applied Mathematics and Statistics*, vol. 2, p. 7, 2016.

52. M. A. Schwemmer and T. J. Lewis, "Effects of dendritic load on the firing frequency of oscillating neurons," *Physical Review E*, vol. 83, no. 3, p. 031906, 2011.

53. S. M. Crook, G. B. Ermentrout, and J. M. Bower, "Dendritic and synaptic effects in systems of coupled cortical oscillators," *Journal of computational neuroscience*, vol. 5, no. 3, pp. 315–329, 1998.

54. J. A. Goldberg, C. A. Deister, and C. J. Wilson, "Response Properties and Synchronization of Rhythmically Firing Dendritic Neurons," *Journal of Neurophysiology*, vol. 97, pp. 208–219, Jan. 2007.

55. M. W. Remme, M. Lengyel, and B. S. Gutkin, "The role of ongoing dendritic oscillations in single-neuron dynamics," *PLoS Comput Biol*, vol. 5, no. 9, p. e1000493, 2009.

56. G. Major, J. D. Evans, and J. Jack, "Solutions for transients in arbitrarily branching cables: I. voltage recording with a somatic shunt," *Biophysical journal*, vol. 65, no. 1, pp. 423–449, 1993.

57. W. A. Wybo, K. M. Stiefel, and B. Torben-Nielsen, "The green's function formalism as a bridge between single-and multi-compartmental modeling," *Biological cybernetics*, vol. 107, no. 6, pp. 685–694, 2013.

58. W. A. Wybo, J. Jordan, B. Ellenberger, U. M. Mengual, T. Nevian, and W. Senn, "Data-driven reduction of dendritic morphologies with preserved dendro-somatic responses," *Elife*, vol. 10, 2021.

59. Y. Wei, G. Ullah, and S. J. Schiff, "Unification of neuronal spikes, seizures, and spreading depression," *Journal of Neuroscience*, vol. 34, no. 35, pp. 11733–11743, 2014.

60. D. Depannemaecker, A. Ivanov, D. Lillo, L. Spek, C. Bernard, and V. Jirsa, "A unified physiological framework of transitions between seizures, sustained ictal activity and depolarization block at the single neuron level," *Journal of computational neuroscience*, vol. 50, no. 1, pp. 33–49, 2022.

61. B. F. Behabadi, A. Polsky, M. Jadi, J. Schiller, and B. W. Mel, "Location-dependent excitatory synaptic interactions in pyramidal neuron dendrites," *PLoS computational biology*, vol. 8, no. 7, p. e1002599, 2012.

62. A. Tzilivaki, G. Kastellakis, and P. Poirazi, "Challenging the point neuron dogma: Fs basket cells as 2-stage nonlinear integrators," *Nature communications*, vol. 10, no. 1, pp. 1–14, 2019.

63. A. Gidon, T. A. Zolnik, P. Fidzinski, F. Bolduan, A. Papoutsi, P. Poirazi, M. Holtkamp, I. Vida, and M. E. Larkum, "Dendritic action potentials and computation in human layer 2/3 cortical neurons," *Science*, vol. 367, no. 6473, pp. 83–87, 2020.

64. A. Stöckel and C. Eliasmith, "Computational properties of multi-compartment lif neurons with passive dendrites," *Neuromorphic Computing and Engineering*, 2022.

65. X.-J. Wang and G. Buzsáki, "Gamma oscillation by synaptic inhibition in a hippocampal interneuronal network model," *Journal of neuroscience*, vol. 16, no. 20, pp. 6402–6413, 1996.

66. W. R. Holmes and C. D. Woody, "Effects of uniform and non-uniform synaptic 'activation-distributions' on the cable properties of modeled cortical pyramidal neurons," *Brain research*, vol. 505, no. 1, pp. 12–22, 1989.

67. M. Häusser and B. A. Clark, "Tonic synaptic inhibition modulates neuronal output pattern and spatiotemporal synaptic integration," *Neuron*, vol. 19, no. 3, pp. 665–678, 1997.

68. M. Rudolph and A. Destexhe, "A fast-conducting, stochastic integrative mode for neocortical neurons invivo," *Journal of Neuroscience*, vol. 23, no. 6, pp. 2466–2476, 2003.

69. C. Koch, "Cable theory in neurons with active, linearized membranes," *Biological Cybernetics*, vol. 50, no. 1, pp. 15–33, 1984.

70. S. Coombes, Y. Timofeeva, C.-M. Svensson, G. J. Lord, K. Josić, S. J. Cox, and C. M. Colbert, "Branching dendrites with resonant membrane: a "sum-over-trips" approach," *Biological Cybernetics*, vol. 97, no. 2, pp. 137–149, 2007.

71. M. W. Remme and J. Rinzel, "Role of active dendritic conductances in subthreshold input integration," *Journal of computational neuroscience*, vol. 31, no. 1, pp. 13–30, 2011.

72. E. Zhuchkova, M. W. Remme, and S. Schreiber, "Somatic versus dendritic resonance: differential filtering of inputs through non-uniform distributions of active conductances," *PLoS One*, vol. 8, no. 11, p. e78908, 2013.

73. N. W. Schultheiss, J. R. Edgerton, and D. Jaeger, "Phase response curve analysis of a full morphological globus pallidus neuron model reveals distinct perisomatic and dendritic modes of synaptic integration," *Journal of Neuroscience*, vol. 30, no. 7, pp. 2767–2782, 2010.

74. M. E. Larkum, J. Wu, S. A. Duverdin, and A. Gidon, "The guide to dendritic spikes of the mammalian cortex in vitro and in vivo," *Neuroscience*, 2022.

75. M. E. Larkum, J. J. Zhu, and B. Sakmann, "A new cellular mechanism for coupling inputs arriving at different cortical layers," *Nature*, vol. 398, no. 6725, pp. 338–341, 1999.

76. S. R. Williams and G. J. Stuart, "Mechanisms and consequences of action potential burst firing in rat neocortical pyramidal neurons," *The Journal of physiology*, vol. 521, no. Pt 2, p. 467, 1999.

77. C. Grienberger, X. Chen, and A. Konnerth, "Nmda receptor-dependent multidendrite ca2+ spikes required for hippocampal burst firing in vivo," *Neuron*, vol. 81, no. 6, pp. 1274–1281, 2014.

78. G. Yi, J. Wang, X. Wei, and B. Deng, "Action potential initiation in a two-compartment model of pyramidal neuron mediated by dendritic ca2+ spike," *Scientific Reports*, vol. 7, no. 1, pp. 1–16, 2017.

79. M. H. P. Kole and G. J. Stuart, "Signal Processing in the Axon Initial Segment," *Neuron*, vol. 73, no. 2, pp. 235–247, 2012.

80. M. S. Hamada, S. Goethals, S. I. D. Vries, R. Brette, and M. H. P. Kole, "Covariation of axon initial segment location and dendritic tree normalizes the somatic action potential," *PNAS*, vol. 113, no. 51, 2016.

81. S. Goethals and R. Brette, "Theoretical relation between axon initial segment geometry and excitability," *Elife*, vol. 9, p. e53432, 2020.

82. C. Zhang, D. Hofmann, A. Neef, and F. Wolf, "Ultrafast population coding and axo-somatic compartmentalization," *PLoS computational biology*, vol. 18, no. 1, p. e1009775, 2022.

83. Y. A. Kuznetsov, "Elements of applied bifurcation theory," vol. 112, ch. 8, pp. 293–392, Springer Science & Business Media, 2013.

84. C. Rackauckas and Q. Nie, "Differentialequations.jl–a performant and feature-rich ecosystem for solving differential equations in julia," *Journal of Open Research Software*, vol. 5, no. 1, 2017.

85. J. Bezanson, A. Edelman, S. Karpinski, and V. B. Shah, "Julia: A fresh approach to numerical computing," *SIAM review*, vol. 59, no. 1, pp. 65–98, 2017.

86. J. G. Verwer and J. M. Sanz-Serna, "Convergence of method of lines approximations to partial differential equations," *Computing*, vol. 33, no. 3-4, pp. 297–313, 1984.

87. "Julianlsolvers/nlsolve.jl: v4.5.1 (v4.5.1)," 2020.

88. E. J. Doedel, A. R. Champneys, T. Fairgrieve, Y. Kuznetsov, B. Oldeman, R. Paffenroth, B. Sandstede, X. Wang, and C. Zhang, "Auto-07p: Continuation and bifurcation software for ordinary differential equations (2007)," *Available for download from http://indy. cs. concordia. ca/auto*, 2007.

89. E. L. Allgower and K. Georg, *Numerical continuation methods: an introduction*, vol. 13. Springer Science & Business Media, 2012.